Investigating processes influencing simulation of local Arctic wintertime anthropogenic pollution in Fairbanks, Alaska, during ALPACA-2022

Natalie Brett[1,2], Kathy S. Law[1], Steve R. Arnold[2], Javier G. Fochesatto[3], Jean-Christophe Raut[1],
Tatsuo Onishi[1], Robert Gilliam[4], Kathleen Fahey[4], Deanna Huff[5], George Pouliot[4], Brice Barret[6],
Elsa Dieudonné[7], Roman Pohorsky[8], Julia Schmale[8], Andrea Baccarini[8,9], Slimane Bekki[1],
Gianluca Pappaccogli[10], Federico Scoto[10], Stefano Decesari[11], Antonio Donateo[10],
Meeta Cesler-Maloney[12], William Simpson[12], Patrice Medina[6], Barbara D'Anna[13],
Brice Temime-Roussel[13], Joel Savarino[14], Sarah Albertin[14,1], Jingqiu Mao[12], Becky Alexander[15],
Allison Moon[15], Peter F. DeCarlo[16], Vanessa Selimovic[17], Robert Yokelson[18], and Ellis S. Robinson[16]

[1]Sorbonne Université, UVSQ, CNRS, LATMOS, 75252 Paris, France
[2]Institute for Climate and Atmospheric Science, School of Earth and Environment,
University of Leeds, Leeds, UK
[3]Department of Atmospheric Sciences, College of Natural Science and Mathematics, University of Alaska
Fairbanks, Fairbanks, AK 99775, United States
[4]Center for Environmental Measurement and Modeling, Office of Research and Development, US EPA,
Research Triangle Park, NC 27709, United States
[5]Alaska Department of Environmental Conservation, P.O. Box 111800, Juneau, AK 99811-1800, United States
[6]Laboratoire d'Aérologie (LAERO), Université Toulouse III – Paul Sabatier,
CNRS, 31400 Toulouse, France
[7]Laboratoire de Physico-Chimie de l'Atmosphère (LPCA), Université du Littoral Côte d'Opale
(ULCO), 59140 Dunkirk, France
[8]Extreme Environments Research Laboratory, École Polytechnique Fédérale de Lausanne,
Sion, 1950, Switzerland
[9]Laboratory of Atmospheric Processes and their Impacts, École Polytechnique Fédérale de Lausanne,
Lausanne, 1015, Switzerland
[10]Institute of Atmospheric Sciences and Climate (ISAC) of the National Research Council
of Italy (CNR), Lecce 73100, Italy
[11]Institute of Atmospheric Sciences and Climate (ISAC) of the National Research Council
of Italy (CNR), Bologna 40121, Italy
[12]Geophysical Institute and Department of Chemistry and Biochemistry, University of Alaska Fairbanks,
Fairbanks, AK 99775, United States
[13]Aix Marseille Univ, CNRS, LCE, 13331 Marseille, France
[14]IGE, Univ. Grenoble Alpes, CNRS, INRAE, IRD, Grenoble INP, 38000 Grenoble, France
[15]Department of Atmospheric and Climate Science, University of Washington,
Seattle, WA 98195, United States
[16]Department of Environmental Health and Engineering, Johns Hopkins University,
Baltimore, MD 21218, United States
[17]Department of Chemistry, University of Michigan, Ann Arbor, MI 48109, United States
[18]Department of Chemistry and Biochemistry, University of Montana, Missoula, MT 59812, United States

Correspondence: Natalie Brett (natalie.brett@latmos.ipsl.fr) and Steve R. Arnold (s.arnold@leeds.ac.uk)

Abstract. CE1 Lagrangian tracer simulations are deployed to investigate processes influencing vertical and horizontal dispersion of anthropogenic pollution in Fairbanks, Alaska, during the Alaskan Layered Pollution and Chemical Analysis (ALPACA) 2022 field campaign. Simulations of carbon monoxide (CO), sulfur dioxide (SO_2), and nitrogen oxides (NO_x), including surface and elevated sources, are the highest at the surface under very cold stable conditions. Pollution enhancements above the surface (50–300 m) are mainly attributed to elevated power plant emissions. Both surface and elevated sources contribute to Fairbanks' regional pollution that is transported downwind, primarily to the south-west, and may contribute to wintertime Arctic haze. Inclusion of a novel power plant plume rise treatment that considers the presence of surface and elevated temperature inversion layers leads to improved agreement with observed CO and NO_x plumes, with discrepancies attributed to, for example, displacement of plumes by modelled winds. At the surface, model results show that observed CO variability is largely driven by meteorology and, to a lesser extent, by emissions, although simulated tracers are sensitive to modelled vertical dispersion. Modelled underestimation of surface NO_x during very cold polluted conditions is considerably improved following the inclusion of substantial increases in diesel vehicle NO_x emissions at cold temperatures (e.g. a factor of 6 at −30 °C). In contrast, overestimation of surface SO_2 is attributed mainly to model deficiencies in vertical dispersion of elevated (5–18 m) space heating emissions. This study highlights the need for improvements to local wintertime Arctic anthropogenic surface and elevated emissions and improved simulation of Arctic stable boundary layers.

1 Introduction

Arctic haze, with enhanced aerosols and trace gases, is formed in the lower troposphere during late winter and early springtime (Shaw, 1995) and is predominantly caused by low-level transport of pollution, driven by low-pressure weather systems, originating from northern Eurasia (Stohl, 2006; Bourgeois and Bey, 2011; Law et al., 2014). Declining trends since the early 1990s in aerosol mass concentrations of Arctic haze constituents, including sulfate aerosols and black carbon (BC), across many stations, including Utqiaġvik (formerly Barrow), Alaska, and Alert, Canada, correlate with reductions in anthropogenic emissions in northern mid-latitudes (Bodhaine and Dutton, 1993; Sharma et al., 2019; Schmale et al., 2022). However, increases in Arctic urbanisation and industrial activities, which are anticipated to continue rising due to the warming climate and socio-economic development, also contribute to Arctic haze and to local air quality, highlighting their importance for Arctic urban areas and local communities (Andrew, 2014; Schmale et al., 2018). Local sources of air pollution in the Arctic include gas flaring, mining, shipping, domestic heating, and power generation (Stohl et al., 2013; Schmale et al., 2018). In the wintertime, energy demands are considerable due to the harsh, cold climates endured by residents. However, significant challenges arise when implementing sustainable transportation and energy infrastructure (de Witt et al., 2021; Kolker et al., 2022) due to remote and sparsely populated communities and cities (Schmale et al., 2018). This has led to substantial investment in fossil fuel power generation, e.g. in Alaska and Canada (Mortensen et al., 2017; Kolker et al., 2022). The release of harmful air pollutants from surface emission sources and elevated power plant stacks contributes to poor air quality and adverse effects on human health during Arctic winter (Rosenthal and Watson, 2011; Schmale et al., 2018). These effects are exacerbated by snow-covered surfaces and low solar radiation at this time of the year, which create favourable conditions for reduced atmospheric boundary layer (ABL) heights and the formation of surface-based temperature inversions (SBIs). Such strong stratification near the surface inhibits pollution dispersion, leading to a build-up of pollutants at breathing level (Bradley et al., 1992; Shaw, 1995). However, the contribution of local Arctic emissions to air quality and their possible contribution to background Arctic haze remain poorly quantified. This is due to uncertainties in emissions and in the ability of models to capture wintertime processes such as aerosol formation and deposition, as well as complex boundary layer meteorology (Emerson et al., 2020; AMAP, 2021; Donateo et al., 2023).

Fairbanks, a sub-Arctic city in the interior of Alaska (64.8° N, 147.7° W), is an example of a polluted urban area. Despite the relatively low population ($\sim$ 33 000 inhabitants in Fairbanks and 100 000 in Fairbanks North Star Borough (FNSB) agglomeration), the 24 h average National Ambient Air Quality Standard (NAAQS) of 35 µg m^{-3} of particulate matter below 2.5 µm diameter ($PM_{2.5}$) set by the United States Environmental Protection Agency (US EPA) is regularly exceeded during wintertime (Simpson et al., 2019). Primary emissions in Fairbanks in winter are produced from domestic home heating systems, transportation, and power plant combustion sources (ADEC, 2019), with increased demand due to frequent extreme cold episodes. Fairbanks is situated in a semi-open basin, surrounded by hills and valleys to the north, east, and west. This topography, coupled with the regular occurrence of anticyclonic meteorological conditions, sets up strong SBIs induced by strong surface radiative cooling (surface temperatures reaching −40 °C) and near-

surface temperature gradients often exceeding $0.5\,^{\circ}\mathrm{C}\,\mathrm{m}^{-1}$ (Mayfield and Fochesatto, 2013; Malingowski et al., 2014; Ye and Wang, 2020), contributing to very stable meteorological ABL conditions. This favours regional atmospheric blocking (low wind speeds) and hinders pollutant dispersion, leading to elevated surface concentrations (Mölders et al., 2011; Cesler-Maloney et al., 2022). Trapping of pollutants occurs not only at the near surface, but also in laminar layers aloft due to the presence of elevated temperature inversion (EI) layers that can form above SBIs (Angevine et al., 2001; Fochesatto et al., 2001; Mayfield and Fochesatto, 2013). Thus, pollutant emissions from elevated sources, such as power plant chimney stacks, can be influenced by the presence of stably stratified layers (Pasquill and Smith, 1983; Briggs, 1984; Tran and Mölders, 2011; Akingunola et al., 2018). Less stable conditions, with weak surface temperature inversions, can be induced by transient or cyclonic synoptic conditions or local sub-mesoscale flows under anticyclonic conditions (Maillard et al., 2022).

The Alaskan Layered Pollution and Chemical Analysis (ALPACA) project aims to improve understanding about wintertime Arctic air pollution, including attribution of local pollution sources, chemical formation pathways of aerosols under cold and low photochemistry regimes, and pollution transport in the stratified ABL (Simpson et al., 2019). To study these issues, the international ALPACA field campaign took place in Fairbanks in January and February 2022 (ALPACA-2022). The campaign design, measurements, and first results are described in Simpson et al. (2024). Vertical profiles of trace gases and particles collected on a tethered balloon (Helikite) on the western edge of the city showed the regular presence of pollution layers close to the surface and aloft, which emission tracer forecasts during the campaign attributed to power plant emissions (Simpson et al., 2024).

Here, we aim to understand processes influencing the vertical and spatial distributions of air pollutants during the ALPACA-2022 field campaign. We use the FLEXible PARTicle-Weather Research and Forecasting (FLEXPART-WRF) Lagrangian particle dispersion model, driven by meteorological fields from WRF simulations generated by the US EPA. Transport of emission tracers of carbon monoxide (CO), sulfur dioxide (SO_2), nitric oxide (NO), and nitrogen dioxide (NO_2) is simulated in the Fairbanks area, and its dependence on ABL structure and stability is investigated. Three of the selected trace gases (CO, SO_2, and NO_2) are defined as "criteria pollutants" for human health by the US EPA. Simulations include hourly-varying surface and non-surface emissions from the Alaska Department of Environmental Conservation for the US EPA (ADEC) for the campaign period (ADEC, 2023). This includes hourly power plant emissions based on data provided by the power plant operating companies. Buoyancy flux calculations using stack characteristics for each power plant are used to calculate emission injection heights. The presence of temperature inversion layers in the ABL, which can trap power plant

plumes, is also taken into account in a novel approach designed to cap injection heights. Variability in modelled tracers at different altitudes is linked to ABL stability, including the presence of SBIs and EIs. Results are compared to vertical profile data and used to evaluate the power plant plume emission treatments, including plume rise and capping of plumes in multi-layered stratified temperature regimes (Mayfield and Fochesatto, 2013). Simulations are also evaluated against surface data, and the sensitivity of the results to selected processes is explored, including meteorology and emission treatments. This is one of the first studies investigating the role of ABL meteorology in dispersion of elevated and surface emissions in the Arctic wintertime.

The methodology is described in Sect. 2 and includes details about the emissions, power plant plume rise parameterisation, FLEXPART-WRF model configuration, and observations used for the model evaluation. Section 3 provides a brief overview of the ALPACA-2022 campaign, including observations of trace gases and meteorology. Spatial and vertical distributions of modelled emission tracers over the Fairbanks area are presented in Sect. 4. Model results are evaluated against selected vertical profile data in Sect. 5 and surface observations in Sect. 6. The results of the sensitivity runs are also discussed in Sects. 5 and 6. The main findings are presented in Sect. 7 together with wider implications and potential future research avenues.

2 Methodology

FLEXPART-WRF was run from 18 January to 25 February 2022 to explore the transport of local pollution during ALPACA-2022 using high-temporal- and high-spatial-resolution emissions for surface and elevated sources, including emissions from five power plants within the Fairbanks region. Figure 1 shows the power plant, measurement, and analysis locations discussed, together with the areas denoted by FNSB for air quality regulation (AQFairbanks, 2024). For the purposes of this study, the Fairbanks area encompasses Fairbanks and the adjoining town of North Pole. Section 2.1 describes the power plant and surface emissions used in this study. The injection altitude for the power plant releases is estimated according to a plume rise parameterisation, as described in Sect. 2.2. The WRF and FLEXPART-WRF model configurations and control simulations are described in Sect. 2.3, and the observations used for model validation are described in Sect. 2.4. All dates refer to the year 2022.

2.1 Emissions

Selected trace gases from power plant and surface sector emissions provided by the power plant companies and ADEC, respectively, are included in the FLEXPART-WRF simulations. Gridded hourly emission fluxes for CO, SO_2, NO, and NO_2 were developed with the Sparse Matrix Opera-
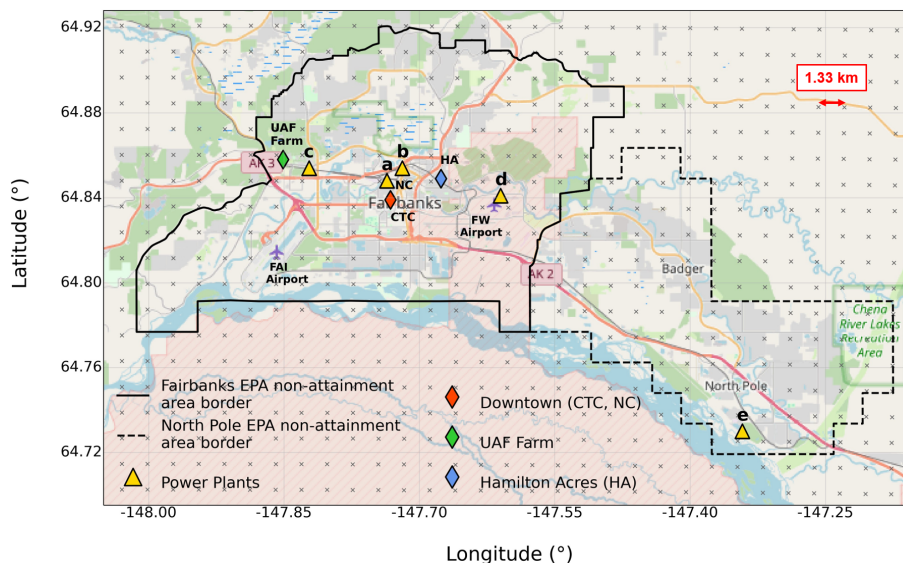
Figure 1. Map of Fairbanks and North Pole. The solid and dashed lines indicate the Fairbanks and North Pole non-attainment areas (AQFairbanks, 2024). The power plant locations (yellow triangles) correspond to the following power plants: **(a)** Aurora, **(b)** Zehnder, **(c)** University of Alaska Fairbanks (UAF), **(d)** Doyon (Fort Wainwright), and **(e)** North Pole. Measurement sites at which trace gas measurements are available for model evaluation are indicated (see Sect. 2.3.1 for details). Two airports, Fairbanks International Airport (FAI) and Fort Wainwright (military base), are also indicated. The grid cells for surface-emitted emissions, 1.33 km apart, are shown as small grey crosses. © OpenStreetMap contributors 2024. Distributed under the Open Data Commons Open Database License (ODbL) v1.0.

tor Kernel Emissions (SMOKE) processing system and data provided by ADEC for the duration of the campaign (CMAS Center, 2023). Tracers of CO, SO_2, and NO_x ($NO + NO_2$) emissions are released from point sources and the near-surface sources with masses based on their respective emissions. These trace gases are chosen based on the availability of emission data and vertical profile and surface observations for model validation. Additionally, it is informative to compare reactive trace gases (SO_2 and NO_x) with CO, which is a good tracer of transport and dispersion due to its long photochemical lifetime.

2.1.1 Power plant emissions

The power plants included in the model simulations are listed in Table 1 together with key stack parameter information, including stack heights, fuel types, flue gas exit temperatures, and velocities. For the five power plant facilities, there are eight stacks included as separate point source releases in FLEXPART-WRF because the UAF and North Pole facilities have more than one power plant stack with variable characteristics that influence the plume buoyancy calculations (Sect. 2.2). Each power plant provided temporal emission information throughout the ALPACA-2022 campaign (see Fig. A2), with the exception of Doyon (coal power plant at Fort Wainwright army base), where hourly 2020 data are used instead. Emissions for each power plant stack are provided at hourly time resolution, except for UAF A and B, for which only daily variability is available. Due to operational

issues, the newer, more efficient coal UAF C stack (64 m height, Table 1) only ran from 4 February (09:00 Alaskan Standard Time, AKST) onward with hourly emissions provided. Prior to this, UAF A and B diesel generators (20 m heights) ran from 17 January but with very low emissions from 1 February. Zehnder was operating only during 4 d in January, and from 10 to 22 February, the operating periods were more frequent. CE2

Figure 2 shows average hourly emissions of CO, SO_2, NO, and NO_2 during ALPACA-2022 for each stack. Overall, Doyon and Aurora contribute the most to SO_2 emissions; UAF C, Doyon, and Aurora (coal-fired plants) contribute the most to CO emissions; and North Pole A, Doyon, and Aurora contribute the most to NO emissions. North Pole A has notably high NO_x emissions because naphtha fuel has high nitrogen content and high NO_x emission potential. Appendix A1 provides information about emission control strategies contributing to these differences. However, temporal emission variations and differences in stack characteristics also affect whether a particular power plant influences trace gas distributions.

2.1.2 Surface emissions

Surface emissions on 1.33 km horizontal grid spacing are provided by ADEC for different sectors. Space heating emissions include commercial and residential sources using coal, distillate oil, gas, and wood, as well as industrial waste oil. The emissions are distributed over the first four WRF

Table 1. Power plant key characteristics. A, B, and C denote separate burners and stacks at the same power plant facility. Locations of power plants are shown in Fig. 1.

Power plant	Stack height (m)	Fuel type	Flue gas exit temperature (°C)	Flue gas exit velocity (m s^{-1})
Aurora	48	Coal	149	78.5
Zehnder	18	Diesel	480	146
UAF A	20	Diesel	149	18.9
UAF B	20	Diesel	177	60.1
UAF C	64	Coal	129	23.4
Doyon	26	Coal	186	38.4
North Pole A	34	Naphtha	202	70.6
North Pole B	19	Diesel	292	176
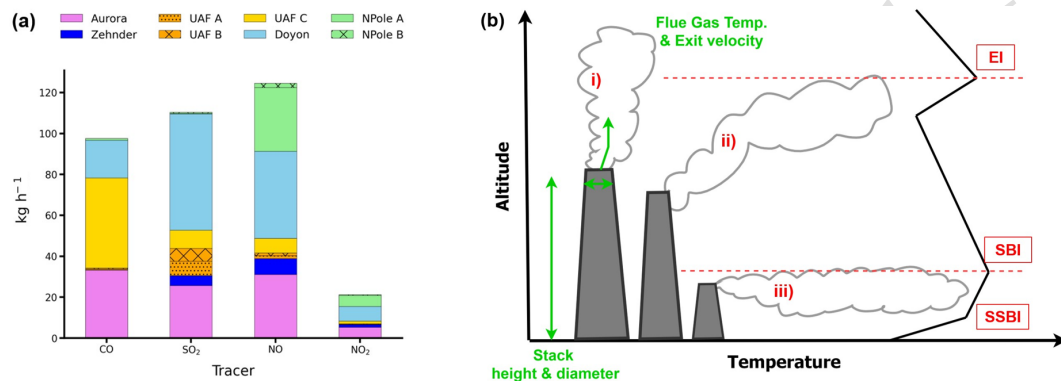
Figure 2. (a) Average power plant emissions (kg h^{-1}) during ALPACA-2022 for CO, SO$_2$, NO, and NO$_2$. **(b)** Schematic illustrating the plume rise parameterisation used to simulate power plant injection altitudes. Examples of surface-based inversion (SBI), stratified SBI (SSBI), and elevated inversion (EI) layers are given and (i) correspond to a plume with no inversion capping, (ii) a plume which has been capped at an EI top, and (iii) a plume which has been capped at an SBI top.

model layers with the following fractions used by EPA: 15 %, 0–4 m; 69 %, 4–8 m; 15 %, 8–12 m; and 0.01 %, 12–18 m. These emissions are then processed by SMOKE according to ALPACA-2022 ambient temperatures. All other emissions are based on 2020 surrogates. On-road and off-road mobile sources take weekday and weekend differences into account and are emitted at the surface (0–4 m). Likewise, non-point sources, including stationary fuel combustion, commercial cooking, and solvent use, are also emitted between 0–4 m. Airport emissions are available on the 38 WRF model levels but are included from 0 to 18 m (first four levels) for the purpose of this study.

Further details about the surface emissions can be found in the ADEC emissions manual (ADEC, 2019). Average emissions for CO, SO$_2$, NO, and NO$_2$ for each sector, summed over the Downtown, Hamilton Acres (HA), UAF Farm, and Fairbanks non-attainment areas between 0–18 m, are shown in Fig. A1.

2.2 Plume rise parameterisation

Air pollutants released from a power plant stack have a buoyancy flux that is dependent on stack parameters (height, radius, flue gas exit temperature, and velocity), along with ambient winds and temperatures in the proximity of the stack (Pasquill and Smith, 1983; Briggs, 1984; Akingunola et al., 2018). This information is required to more realistically predict plume injection altitudes (Bieser et al., 2011; Mailler et al., 2013; Guevara et al., 2014). Thus, power plant plume rise varies temporally depending on power plant operations and local meteorology, in particular related to atmospheric stability and the presence of temperature inversion layers in the Arctic winter. The plume rise parameterisation used here is summarised by the schematic in Fig. 2b and is based on the Briggs (1984) plume rise equations in stable conditions (Eqs. 1 and 2) where the buoyancy flux, denoted F_b (units = m^4 s^{-3}), is given by

$$F_b = \frac{g}{\pi} \times (V \times \frac{T_s - T_a}{T_s}), \quad (1)$$

where g is acceleration due to gravity ($9.81\,\mathrm{m\,s^{-2}}$), T_s is effluent temperature, T_a is ambient temperature at stack height, and V is the volume flow rate ($\mathrm{m^3\,s^{-1}}$) of the effluent, which is equivalent to $v \times r^2$, where v is the exit velocity, and r is the stack radius. The estimated plume rise height, d_h, is then given by

$$d_h = 2.61 \times \left(\frac{F_b}{U_s}\right)^{\frac{1}{3}}, \tag{2}$$

where U_s corresponds to wind speed at the closest altitude of the radiosonde profile to the power plant stack height.

Stack parameters, combined with ambient temperatures and winds at the closest altitude to the stack height, interpolated from the Fairbanks International Airport (FAI) radiosonde profiles, are used to calculate new injection altitudes above the stack height every 12 h at 03:00 and 15:00 Alaskan Standard Time (AKST). For three missing radiosonde profiles, the assumption is made that the atmospheric profile has similar characteristics to the previous profile. The airport is 2 to 12 km from the Fairbanks power plant facilities and ~ 25 km from the North Pole facility.

Diagnosis of plume rise injection heights is further complicated by the vertically stratified ABL in Fairbanks wintertime since the presence of SBIs or EIs can inhibit plume rise and cap the emissions. Although the plume rise calculation given in Eqs. (1) and (2) is generally appropriate for stable conditions, it is not necessarily representative of the extremely stable conditions that occur in winter in Fairbanks with a high-latitude continental climate. SBIs are extremely shallow throughout ALPACA-2022 where the 25th, 50th, and 75th percentiles of SBI top heights determined from FAI radiosondes are 21, 46, and 89 m, respectively. Stratified SBI (SSBI) layers within the SBIs can also develop close to the surface with even steeper positive temperature gradients, as well as EIs aloft, as depicted in Fig. 2 and discussed further in Sect. 3.

In order to take into account possible capping of power plant emissions at the injection (stack) location, the occurrence of SSBIs, SBIs, and/or EIs is diagnosed from the FAI radiosondes every 12 h. A layer fit routine is applied to the radiosonde profiles up to 3000 m to smooth the temperature profiles and assign temperature gradients (dT), according to Fochesatto (2015). Once this is applied, the inversion layer diagnosis is performed, based on the following conditions for each profile:

– Profiles with negative temperature gradients, i.e. no surface or elevated inversions detected, are removed from the analysis.

– SBIs are assigned at the first change in sign of dT away from the surface (from positive to negative).

– EIs are assigned based on layers above the SBI, again when the sign of dT of the next layer changes from positive to negative.

– SSBIs are assigned if there is at least one layer below the SBI and if the gradient changes between the SBI top and the surface but remains positive. If there is more than one layer using this description, the sub-layer with the steepest gradient is assigned as the SSBI.

For each diagnosed inversion layer, the temperature and altitudes at the top of the layer are assigned. Derived 12-hourly SBI and SSBI altitudes are shown in Fig. 3d and discussed further in Sect. 3. Injection heights for the power plant emissions are capped at the top of the diagnosed inversion layers in the control (CTRL) simulation only when the inversion height exceeds the stack height. Otherwise, the EI top aloft is used, if diagnosed. Emission tracers are released between $\pm 8\%$ of the calculated plume rise height to represent the plume thickness. This threshold was chosen based on the optimal thickness compared to observed plumes in test simulations. In the case of plume capping, this also accounts for a small fraction of the emissions penetrating the temperature inversion. Modelled power plant tracers are compared to available vertical profile observations in Sect. 5. The sensitivity of the results to plume rise injection height and capping is also examined.

2.3 Model simulations

This section provides details about the WRF and FLEXPART-WRF model configurations and the tracer simulations.

2.3.1 WRF configuration

The dispersion of emission tracers released in the FLEXPART-WRF simulations is driven by hourly meteorology fields from WRF model simulations provided by the US EPA for the ALPACA-2022 campaign (EPA-WRF from now on) at 1.33 km horizontal resolution with 38 vertical levels. A total of 12 levels are in the lowest 555 m, with 3 below 10 m (Gilliam et al., 2023). The physics parameterisations used are the Rapid Update Cycle land surface model (Benjamin et al., 2004), the Mellor–Yamada–Nakanishi–Niino (MYNN) planetary boundary layer scheme (Nakanishi and Niino, 2009), the Rapid Radiative Transfer Model (RRTM) shortwave (SW) and longwave (LW) radiation (Iacono et al., 2008) scheme, and explicit grid-scale hydrometeors using the Morrison microphysics scheme (Morrison et al., 2009). Observational nudging is applied using all available near-surface measurements of temperature, humidity, and winds and vertical profiles at a few key measurement sites for the duration of ALPACA-2022. The near-surface observations include the University of Alaska Fairbanks (UAF) Community and Technical College (CTC), which was the main ground-based measurement site during ALPACA-2022; ADEC sites including NCORE (NC), A Street, and Hurst Rd; and standard US weather sites and

Table 2. Summary of the CTRL simulation setup and power plant plume rise sensitivity tests.

Simulation name	Air tracers	Description
CTRL	CO NO_x SO_2 + deposition	Surface and power plant tracers Power plant simulation includes plume rise parameterisation plus capping at diagnosed inversion heights (Sect. 2.2)
NO-CAP	CO NO_x SO_2 + deposition	Power plants only Plume rise parameterisation without capping
NO-RISE	CO NO_x SO_2 + deposition	Power plants only No plume rise parameterisation – emission tracers released at stack height

local measurements from the Meteorological Assimilation Data Ingest System (MADIS) database (MADIS, 2023)[CE3]. The CTC, NC, and UAF locations are shown in Fig. 1. Above the surface, hourly Doppler wind light detection and ranging (lidar) measurements at CTC (18 January–7 February) and the UAF Farm (8–25 February) (Fochesatto et al., 2024), as well as FAI radiosonde data, are assimilated into the EPA-WRF simulations. Finally, nudging to National Centers for Environmental Prediction (NCEP) Global Forecast System (GFS) analyses are included above 300 m every 3 h. An evaluation of EPA-WRF against observations is provided in Appendix B.

2.3.2 FLEXPART-WRF configuration

FLEXPART-WRF is a Lagrangian particle dispersion model used to simulate the transport of atmospheric trace constituents. FLEXPART is often run in backward mode to identify key source areas, in particular for long-range transport studies, e.g. Stohl et al. (2013). Forward simulations are used here to evaluate dispersion of emission tracers and the relation to local- and synoptic-scale meteorology over the Fairbanks area during ALPACA-2022.

The land use and topography data for the simulations are taken from EPA-WRF together with hourly winds and temperatures that drive horizontal and vertical transport of the tracers. The turbulent wind parameterisation in the ABL is either calculated internally using the Hanna scheme based on ABL parameters, including ABL height, Obukhov length, and friction velocity (Hanna, 1984), or calculated externally using prognostic turbulent kinetic energy (TKE) from WRF, which includes internal partitioning of TKE into horizontal and vertical components based on the Hanna scheme surface-layer scaling and local stability (Brioude et al., 2013). Brioude et al. (2013) suggested using the Hanna turbulence scheme in typical mid-latitude environments to ensure a well-mixed ABL, but this is not applicable in conditions where the ABL is stably stratified, as is predominantly the case in Fairbanks during winter. Simulations comparing Hanna (not shown here) and WRF-TKE schemes have

shown that WRF-TKE better captures differences in stability regimes around Fairbanks, for instance changes from stable to less stable conditions during the campaign, and is used here in the control (CTRL) simulation. The ABL mixing height (h_{mix}), sensible heat flux, and friction velocity are calculated in FLEXPART-WRF based on EPA-WRF input fields. h_{mix} has a default minimum height (h_{min}) of 100 m. If h_{mix} is calculated to be lower than h_{min}, it is set equal to h_{min}. However, FLEXPART-WRF is generally used in conditions where strong stratification is not a distinct feature with more sunlight, turbulence, and stronger ABL mixing. Since FLEXPART-WRF is not currently configured for use in strongly stable conditions, h_{min} is used here as a proxy to investigate the sensitivity of tracer dispersion to the SBI layer height since it has a strong influence on trapping emissions at or close to the surface. Model simulations are sensitive to h_{min} due to the difficulties in simulating shallow wintertime SSBIs or SBIs in EPA-WRF. h_{min} is set to 20 m in the CTRL configuration rather than 100 m due to better agreement during stable conditions, and the sensitivity to different h_{min} values is explored in Sect. 6.

2.3.3 Tracer simulations

Tracers of CO, SO_2, NO, and NO_2 are released in each simulation based on emissions in the FNSB region, and background concentrations from further afield are not included. Therefore, modelled mixing ratios are enhancements due to Fairbanks local emissions being above background concentrations. For each power plant stack, 5000 particles are released for each tracer, every hour, providing the stack was operational. The total number of particles is scaled by the emission mass and distributed evenly between the particles. Diurnal variability is calculated from the diurnal cycle for each stack. Every 12 h, a new injection height is assigned at the point of emission according to the plume rise parameterisation (Sect. 2.2). For the surface sources, all emission sectors are summed, and an hourly emission variability is assigned to each tracer according to the total sectors; for example the diurnal cycle of CO is comparable to the on-road

mobile sector. A total of 80 000 particles are released every hour over the FNSB non-attainment area. The number of particles in each grid cell depends on the emission mass, which is distributed evenly between all particles. Mobile and non-point-source sectors are released between 0–4 m only, while the space heating and airport emissions are released between 0–4, 4–8, and 8–12 m (also includes layer 4 (12–18 m)). The airport emissions occurring higher than 18 m are not included in this study as they are generally transported to the south-west of the city (see Sect. 4). Modelled tracer concentrations are calculated in volume mixing ratios, allowing for comparison with observed CO, SO_2, and NO_x ($NO + NO_2$) mixing ratios. In CTRL, emitted CO, SO_2, and NO_x are treated as tracers, and atmospheric lifetimes are not included. The influence of meteorology and emission treatments is explored in Sect. 6, together with atmospheric lifetimes (Appendix E5). There is no explicit chemistry or atmospheric lifetime for CO included in the model setup. Dry and wet deposition is CE4 included in CTRL only for SO_2 (see Appendix E3 for more details) since these losses are not important for CO and are considered to be very small for NO_x (Liu et al., 1987). A fog event occurred from 29 January to 3 February (Lill et al., 2024), and precipitation events occurred in February. Runs with and without dry and wet deposition of SO_2 only had a very small influence on the results (not shown). CTRL includes power plant plume rise and capping of plume injection heights, as described in Sect. 2.2. The NO-CAP sensitivity includes power plant plume rise without capping at inversion heights, and, in the NO-RISE sensitivity, emission tracers are released at the height of the stack. Results are discussed in Sect. 5. The CTRL setup and power plant sensitivities are summarised in Table 2.

2.4   Observations

Model simulations are evaluated against surface and vertical profile observations from ALPACA-2022 sites shown in Fig. 1. Further details about measurement techniques, sites, and observations are given in Simpson et al. (2024). Hourly-averaged surface observations of CO, SO_2 at CTC and NC, and NO_x at CTC, as well as wind speeds, wind directions, and temperatures at 3, 11, and 23 m at CTC and 3 and 11 m at NC are used to evaluate FLEXPART-WRF tracer concentrations and EPA-WRF meteorology, respectively, in urban Fairbanks (Downtown in Fig. 1). Surface observations of CO and NO_x at the ALPACA-2022 house site in Hamilton Acres (HA), in the eastern residential area of Fairbanks, together with surface CO and meteorological parameters (2.5 m winds and 2 and 11 m temperatures) at the UAF Farm site in the west of the city, are also used.

In situ vertical profiles were measured at the UAF Farm site using the École Polytechnique Fédérale de Lausanne (EPFL) Helikite, a tethered balloon stabilised by a kite, from the surface up to 350 m (Pohorsky et al., 2024a). Here, profiles of temperature, NO_x, and CO, measured using the Mi-cromegas low-cost sensor package at 15 s time resolution and calibrated using machine learning algorithms (Barret et al., 2024a), CE5 are used, as well as EPFL mid-infrared absorption (MIRA) Pico CO data. EPFL CO_2 profiles measured by the Vaisala GMP343 are used to check pollution presence observed in the trace gas profiles, since we expect CO_2 profile measurements to be highly reliable due to the stability of the Vaisala instrument. More details about the EPFL instruments are provided in Pohorsky et al. (2024b). All Helikite observations are averaged over 15 s time resolution for consistency. Temperature profiles from the FAI radiosondes at 15:00 and 03:00 AKST are used to complement the analysis. Wind lidar attenuated backscatter data are also used to detect pollution (aerosol) plume presence between 40 and 290 m (see Appendix D2 for details).

At the surface (0–25 m), strongly stable (SS) and weakly stable (WS) meteorological regimes are diagnosed based on observed temperature gradients $\left(\frac{dT}{dZ}\right)$ per 100 m calculated using the 12-hourly FAI radiosonde data. To improve the temporal resolution, temperature gradients (dT 23–3 m) at CTC, with hourly resolution (shown in Fig. 3c), are also used to account for variability not captured in the 12-hourly data. Criteria based on previous studies, including Cesler-Maloney et al. (2022) and Malingowski et al. (2014), are used to determine SS or WS regimes (see Table 3).

3   Meteorological variability during the ALPACA-2022 campaign

Figure 3 shows the time series of observed surface NO_x, wind speeds, temperature gradients, and stability analysis at the CTC site in central Fairbanks and surface pressure at the UAF Farm during ALPACA-2022. Overall, anticyclonic conditions were frequent during the campaign, resulting in cold, calm, and generally clear-sky conditions (Simpson et al., 2024). This coincides with the presence of SBIs, high NO_x concentrations, and generally lower wind speeds near the surface (Fig. 3, panels a–c). Due to a large-scale synoptic variability during the campaign, anticyclonic conditions were interspersed with less stable conditions. This was due to the intrusion of low-pressure weather systems over central Alaska, notably during February. During these conditions, weaker SBIs, lower NO_x, and higher surface wind speeds were observed. Figure 3 variables (panels a–c) are coloured according to SS or WS regimes. Most notably, SS conditions prevailed in periods with strong positive surface temperature gradients, resulting in higher NO_x. The presence of SBIs, SSBIs, and EIs is also diagnosed in FAI radiosonde profiles, as described in Sect. 2.2, and SBI and SSBI top heights are shown in Fig. 3d. SBI top heights range between 7 and > 200 m and are the lowest during SS conditions (often below 30 m). The presence of stable layers aloft is also detected in radiosonde data up to 300 m, providing information about ABL stability (Fig. 3e), and these data are used in the eval-
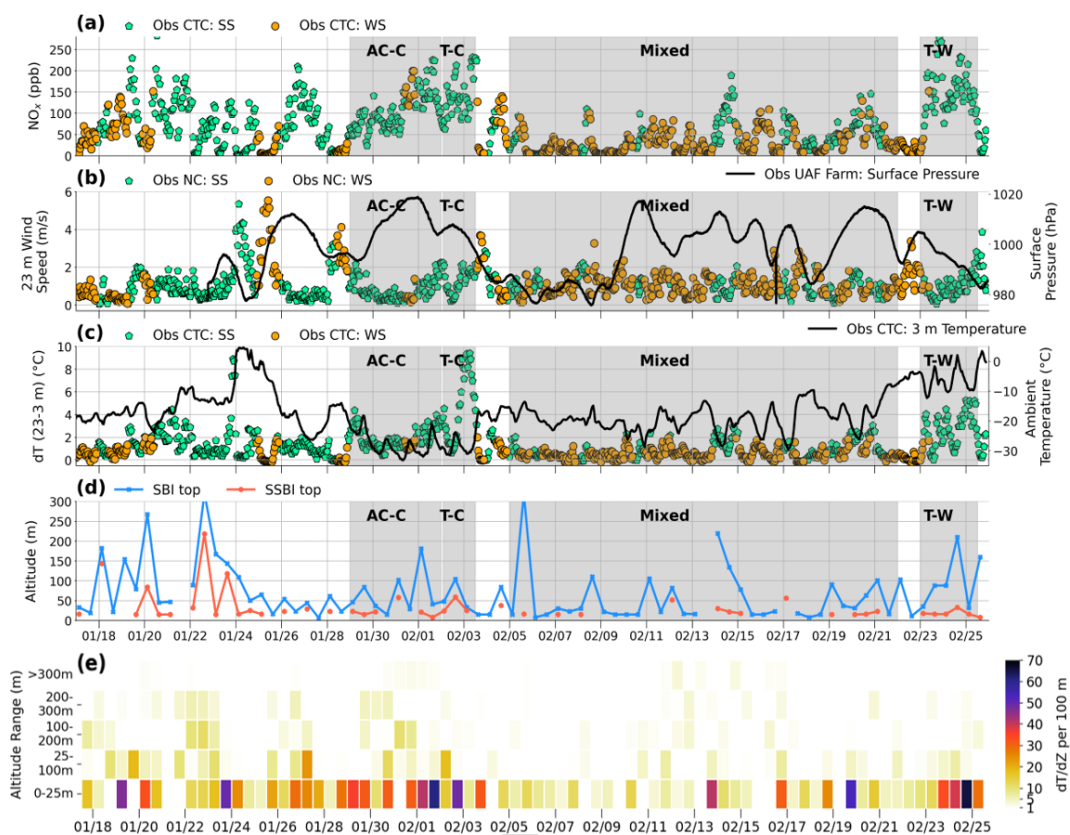
Figure 3. [TS1] Observations of **(a)** surface NO_x mixing ratios (parts per billion, ppb), **(b)** wind speeds (23 m, m s^{-1}) and surface pressure (hPa) at the UAF Farm, and **(c)** temperature inversions (dT 23–3 m, °C) at CTC during the ALPACA-2022 campaign (1 h averages), coloured by strongly stable (SS) and weakly stable (WS) regimes. **(d)** SBI and SSBI heights (m) derived from the FAI radiosondes (12-hourly) and **(e)** stability strengths, $\frac{dT}{dZ}$ per 100 m (°C (100 m)$^{-1}$) derived from 12-hourly radiosonde data over given altitude bins. The meteorological periods used in the analysis are also indicated in panels **(a)**–**(d)**. See text for details.

Table 3. Surface-level [CE6] stability classifications derived from temperature gradients.

Strongly stable (SS)	Weakly stable (WS)
$\frac{dT}{dZ}$ per 100 m ≥ 10 °C or $\frac{dT}{dZ}$ per 100 m < 10 °C and dT 23–3 m ≥ 2 °C	$\frac{dT}{dZ}$ per 100 m < 10 °C and dT 23–3 m < 2 °C

uation of the model results. For instance, days with strong stability in the surface layer (0–25 m) and weaker stability aloft (> 25 m), such as 24 January, indicate a decoupling of the surface layer from EIs aloft that are linked to large-scale meteorology. By 25 January, the large-scale synoptic conditions influence the surface level, as shown by weak temperature gradients and substantial reductions in surface pollution (e.g. NO_x, panel a). The range of stability strengths shown for the surface layer also enables weaker and stronger SBIs and SSBIs to be distinguished, as shown in Fig. 3e.

In addition to stability regimes, the results are discussed in relation to three periods representative of the dominant meteorological situations that occurred during ALPACA-2022. The first period from 29 January to 3 February occurred when SS conditions dominated at the surface, and EIs were present aloft (Figs. 3d and e). Cold anticyclonic conditions persisted from 29 January to 1 February (named anticyclonic-cold (AC–C)), followed by a transition from AC to cyclonic conditions (or transient-cold (T–C)) from 2–3 February, as shown by a decrease in surface pressure in Fig. 3b. During the T–C period, the high-pressure system that was positioned over interior Alaska during AC–C was interrupted by the northward movement of the Aleutian low-pressure system, resulting in a high–low pressure gradient. The surface layer was decoupled from aloft, with SS conditions persisting at the surface, as shown by strong surface stability strengths (30–60 °C per 100 m, Fig. 3e) and by SBIs or SSBIs often below 30 m (Fig. 3d). The second period, from 23

to 25 February, encompassed a transition from anticyclonic to cyclonic conditions with warmer temperatures compared to T–C (named transition-warm, T–W). Competing high- and low-pressure weather systems, combined with a reduction in radiative cooling with respect to January, and the presence of high-altitude clouds contributed to warmer temperatures at this time. Intrusion of a warm air mass warmed the layers above the surface layer CE7 and increased the temperature gradients at the surface, as shown by the increased inversion strength at the surface between 24 and 25 February (Fig. 3e)). These SS surface conditions resulted in NO_x exceeding 250 parts per billion (ppb) (Fig. 3a). The third period, from 5 to 21 February, is denoted as the Mixed period, with transient, cyclonic, and anticyclonic large-scale meteorological conditions. SS conditions occurred at the surface but did not persist for longer than 24 h and were interspersed with WS conditions. Enhanced surface pollution coincides with SBI presence, as shown in Fig. 3d.

4 Vertical and horizontal dispersion of emission tracers

Figure 4 shows the total surface-emitted plus power plant tracers of CO and SO_2 from CTRL near to the surface (0–10 m) and for SO_2 aloft (50–100 and 200–300 m) averaged over the whole campaign for SS and WS conditions. Winds are also shown and provide an indication of average wind patterns. Below 10 m, simulated tracers are primarily localised in the main urban centres of Fairbanks and North Pole (non-attainment areas), with concentrations under SS conditions about 2 times higher than under WS conditions (SS CO > 500 ppb, WS CO > 200 ppb). This is due to weaker surface winds during SS conditions with no prevalent wind direction (see also observed and EPA-WRF winds at CTC (Fig. B1)). Tracers below 10 m include surface-emitted sources and elevated sources from space heating, airports, and power plants, in particular by power plant emissions with low stack heights, such as Zehnder (18 m) when capping at a shallow SBI occurs, while plants with higher stacks may be transported downward more intermittently, as discussed in the next section CE8. Spatial differences in CO and SO_2 occur because of differences in the dominant surface emission sectors. Two hot spots with enhanced SO_2 correspond to airport emissions located to the south-west of central Fairbanks (FAI) and the east of downtown Fairbanks (Fort Wainwright army base), as shown in Fig. 1. Simulated SO_2 in downtown Fairbanks is primarily influenced by residential and commercial distillate oil heating sectors contributing > 90 % of surface SO_2 emissions. This is reduced in the wider Fairbanks non-attainment area (∼ 65 %) where airport emissions also contribute ∼ 30 % (Fig. A1). SO_2 is smaller in North Pole, which is mainly influenced by residential heating emissions. CO at 0–10 m is primarily influenced by the on-road mobile emissions sector (Fig. A1).

SO_2 is also simulated more substantially between 50–100 m under SS compared to WS conditions due to the stratification of the ABL and a stronger north-easterly flow, possibly contributing to a wider regional influence. Above 50 m, enhanced concentrations are found around the power plants, suggesting that power plant emissions are the main contributors to SO_2 aloft (50–100 and 200–300 m) (see Fig. C1 for results at 100–200 m). Modelled values are in agreement with long-path differential optical absorption spectrometer (LP-DOAS) SO_2 measurements ranging from 5–15 ppb collected between 73–191 m to the north-east of the Downtown area during polluted periods (Simpson et al., 2024). SO_2 is also influenced by power plant emissions at 200–300 m, with enhancements up to 1–2 ppb. Concentration enhancements are larger during WS conditions, when winds are often north-easterly below 200 m and stronger (> 3 m s^{-1}), compared to SS conditions, when winds are from the east and weaker (< 3 m s^{-1}). At 200–300 m, wind speeds are strong in both WS and SS conditions. Weaker winds in the lower ABL in SS conditions reflect increased stratification and limited vertical transport, with stronger winds and more vertical exchange during WS conditions. However, tracer enhancements are considerably smaller above 200 m, and the bulk of pollution tracers is transported at lower altitudes in dominant north-easterly outflow (to the south-west).

Additional results for CO and NO_x are shown in Figs. C1 and C2, respectively. CO enhancements above 50 m, relative to 0–10 m, are inappreciable compared to SO_2 because CO surface emissions are much larger relative to power plant emissions compared to SO_2. For instance, CO surface emissions (campaign average) in the Fairbanks non-attainment area (approx. 950 kg h^{-1}, Fig. A1a, i) are a factor of 10 higher than total CO power plant emissions (approx. 98 kg h^{-1}, Fig. 2a), whereas the emission masses for SO_2 are comparable in both cases (110–120 kg h^{-1}). Simulated NO_x at 0–10 and 50–100 m shows similar spatial patterns to CO, with surface concentrations of > 50 ppb on average. Emissions are mainly from the on-road mobile sector and, to a lesser extent, residential distillate oil. Power plant emissions also contribute aloft (> 10 ppb at 100–200 m), especially around the North Pole A stack CE9, which runs on naphtha, a fuel high in NO_x emissions (see Fig. C2b).

The vertical distributions of SO_2 from power plant and surface-emitted sources at Downtown and the UAF Farm during the campaign are shown in Fig. 5, and SS or WS conditions are indicated. As shown in Fig. 4, simulated near-surface mixing ratios are enhanced during SS compared to WS conditions. Emission tracers are concentrated in the lowest 20 m, in particular in the Downtown area due to strong vertical stratification. This capping at 20 m is related to running the model with $h_{min} = 20$ m in the FLEXPART-WRF turbulence scheme. Sensitivity of the model results to this parameter is examined further in Sect. 6. In contrast, lower surface concentrations are simulated during WS conditions. They are sometimes linked to stronger vertical
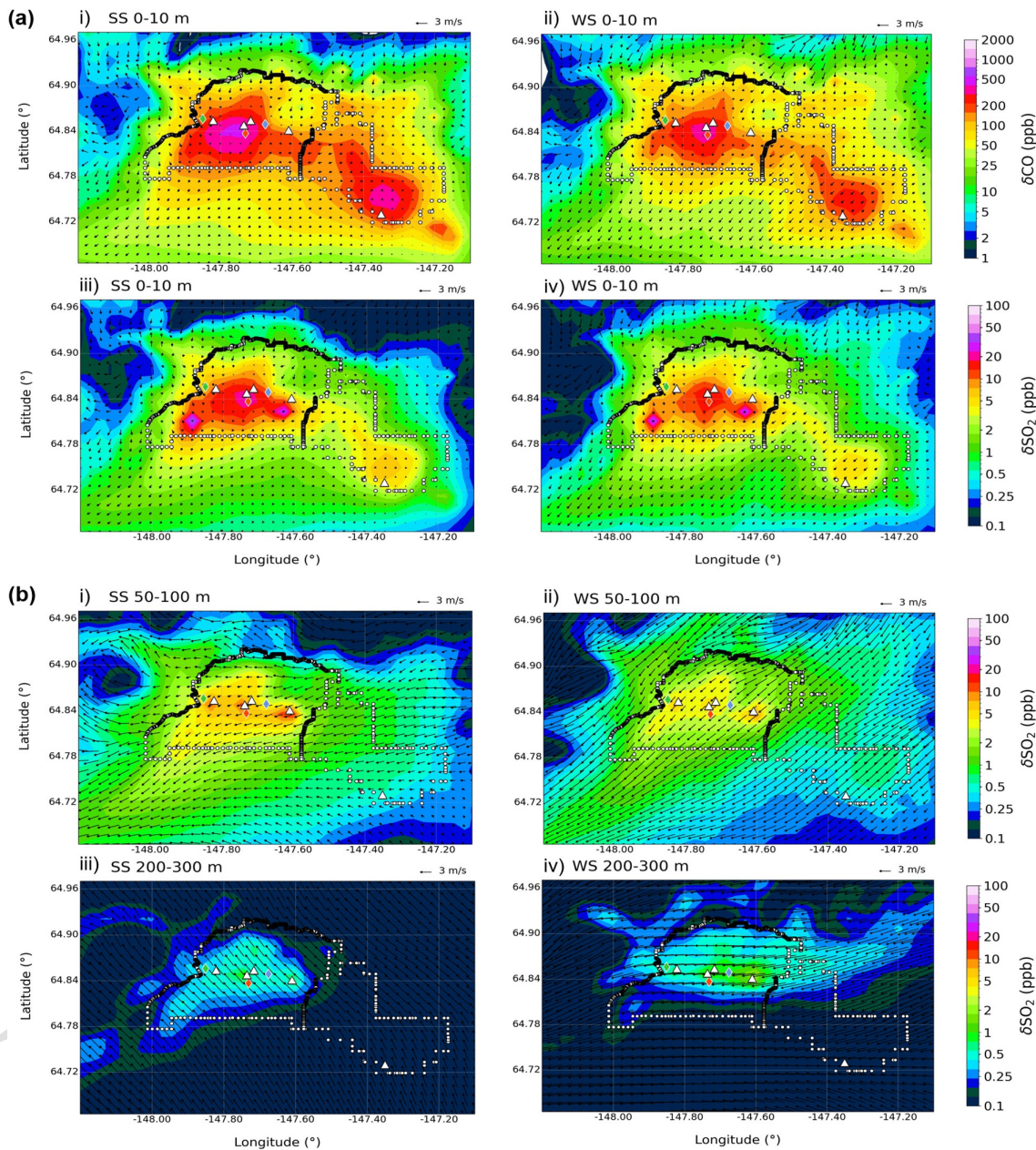
Figure 4. (a) Total power plant and surface-emitted tracers (enhancements above background in ppb) from CTRL for CO and SO_2 at 0–10 m and (b) SO_2 at 50–100 m (i, ii) and 200–300 m (iii, iv) for strongly stable (SS) (left) and weakly stable (WS) (right) meteorological conditions. Wind vectors (black arrows) indicating average wind direction (°) and speeds (m s^{-1}) from EPA-WRF are shown and correspond to respective altitudes. The Fairbanks and North Pole non-attainment area borders are marked with black and white circles, power plants with white triangles, and analysis locations with coloured diamonds, as in Fig. 1.

transport when a higher proportion of SO_2 is lofted upwards up to 300 m, for example on 6–7 and 9–10 February over the Downtown area. In other cases, reduced near-surface SO_2 mixing ratios are explained by enhanced horizontal dispersion, e.g. on 24–25 January and 3–4 February (Downtown), due to stronger wind speeds between 2–6 m s^{-1} (see also Fig. 3b). At the UAF Farm, the model simulates stronger vertical dispersion of both surface and power plant

tracers (Fig. 5b), likely induced by stronger turbulence and wind speeds at this site (see also Fig. B2 showing stronger modelled and observed winds compared to the Downtown sites). At HA, surface-emitted tracers are also maintained near the surface during SS conditions. Vertical transport appears larger than in the Downtown area but smaller than at the UAF Farm, markedly in February, when mixing heights greater than 20 m are depicted (see Fig. C3a).
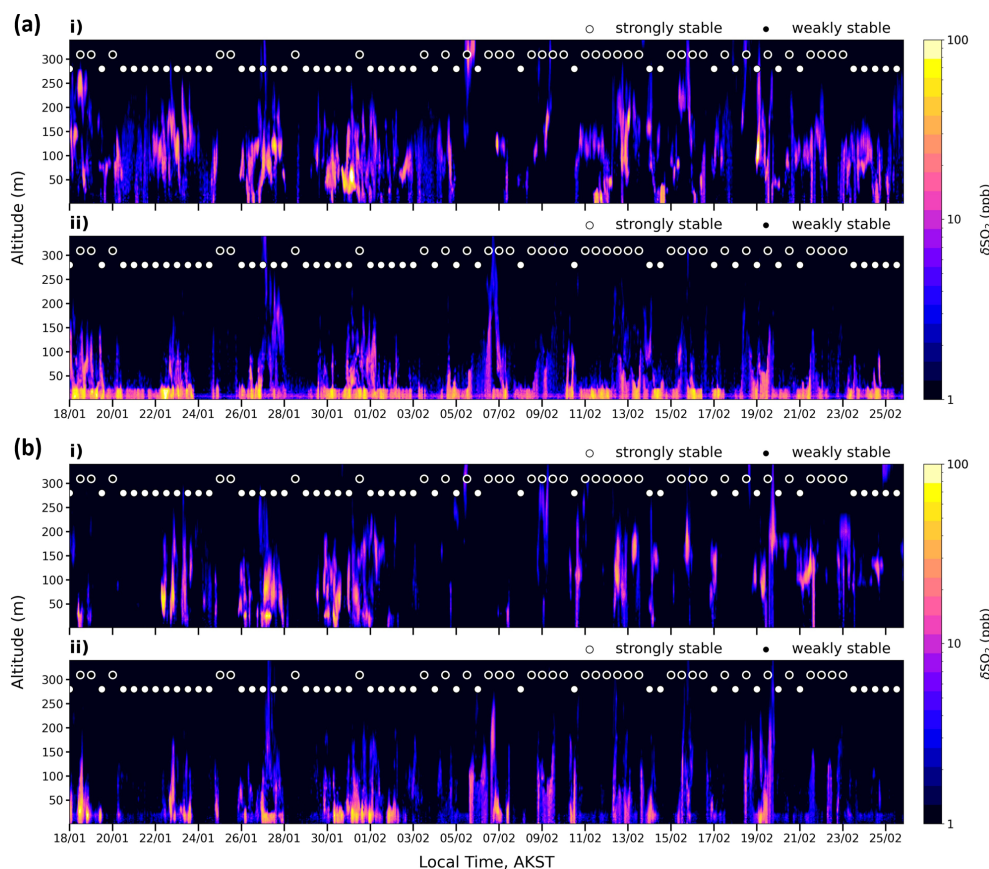
Figure 5. (a) Modelled (CTRL) SO_2 tracer (ppb) as a function of altitude (m) and local time (AKST, hours) for (i) total power plant emissions and (ii) total surface emissions **(a)** Downtown and **(b)** at the UAF Farm. The WS and SS surface stability regimes are indicated every 12 h by filled (solid) and unfilled (open) circles, respectively.

Power plant tracers of SO_2 are generally simulated between 50–250 m over Downtown (Fig. 5a), with some dispersion towards the surface in both SS and WS conditions (e.g. 30 January to 1 February) and enhanced vertical transport in WS conditions. The results also show that power plant SO_2 tracers are simulated at higher altitudes from 4–25 February over the UAF Farm (Fig. 5b). This is due to a change in operations from UAF A and UAF B to the UAF C facility, which has a higher stack height (64 m) and runs on coal instead of diesel, also resulting in higher CO concentrations from power plant emissions during this period (Fig. C3b). Power plant tracers also have a substantial impact at HA (e.g. SO_2, Fig. C3a) and are attributed predominantly to the Doyon stack to the south-east of the site (Fig. 1).

Overall, these results show that pollution is enhanced at the surface. Surface enhancements are considerable under SS conditions, while aloft enhancements can be greater under WS conditions due to more vertical transport. In both cases, the results suggest that background pollution levels are being influenced by local air pollution sources from Fairbanks and North Pole. This regional pollution could be contributing to wintertime Arctic haze, which has lower concentra-

tions of trace gases and aerosols. For example, simulated SO_2 concentrations at Villum in north-east Greenland ranged between 0.1 and 2.2 $\mu g\,m^{-3}$ (approx. 0.1–0.9 ppb) in 2018 and 2019 winter months (Skov et al., 2023). Sulfate concentrations between 0.1 and 0.8 $\mu g\,m^{-3}$ at Alert, Zeppelin, and Villum in January and February 2014 were reported in Ioannidis et al. (2023), while sulfate in downtown Fairbanks ranged between 1–5 $\mu g\,m^{-3}$ during ALPACA-2022 (Moon et al., 2023a).

5 Simulated vertical distributions and power plant plumes

Pollution plumes were regularly intercepted by the Helikite at the UAF Farm above the surface layer (Simpson et al., 2024) and are used here to evaluate simulated vertical transport of tracers and, in particular, the power plant plume rise parameterisation. Selected cases with different meteorological regimes are investigated in more detail. As noted earlier, surface mixing ratios at the UAF Farm are generally reduced compared to central Fairbanks. Differences in synoptic- and local-scale meteorological conditions influence horizontal
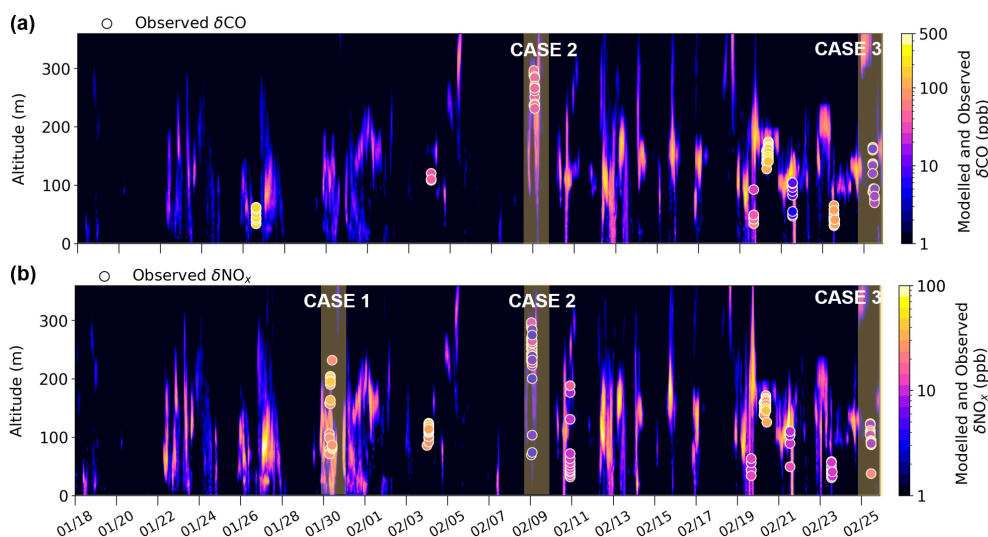
Figure 6. Comparison of modelled (CTRL) power plant and observed trace gas enhancements above background ($> 30\,\text{m}$) for **(a)** δCO (ppb) and **(b)** δNO_x (ppb) at the closest grid cell to the UAF Farm. Observed plume enhancements are shown as circles (ppb). Cases discussed in the main text are highlighted.

and vertical transport at this site together with lower emission magnitudes. However, above about 80 m, there is less influence of local valley flows at the UAF Farm, and wind speeds and directions are more similar to those in central Fairbanks (Fochesatto et al., 2024). Periods with east or north-easterly winds favoured transport of power plant pollution from Fairbanks to the UAF Farm.

Since model results are representative of enhancements above background, a polluted background is assigned to the Helikite CO and NO_x measurements to determine observed pollution plume enhancements (δCO and δNO_x) equivalent to the simulated quantities. First, the pollution plumes are assigned using the 90th TS2 percentile of the distribution of concentrations observed during each flight. A polluted background is assigned using the modal concentration of each flight and subtracted from the identified plume to give the observed pollution plume enhancement (δCO and δNO_x). In order to evaluate power plant plumes only, this comparison only uses observations above 30 m, away from the influence of surface emissions. Some profiles of CO on 30 January and 10 February are removed due to issues with the CO sensor (Barret et al., 2024a).

Figure 6 shows the comparison of model results from CTRL and observed enhancements for each of the identified plumes for CO and NO_x during the campaign when flights took place. CTRL generally captures plume presence aloft when compared with observed δNO_x and δCO above 30 m (Fig. 6a), although there are some displacements that could be due to temporal biases in modelled wind speeds and directions or in the diagnosed injection height. This could be due to using 12-hourly radiosonde data or due to spatial differences, for example using observed profiles at FAI rather

than at each power plant location. In addition, the model is run with an hourly time resolution using EPA-WRF fields, while the Helikite observations are collected at very high temporal resolution. The model is likely to have difficulties in capturing this variability on small spatial scales. To examine the influence of the model treatment of power plant emissions, the model is run without plume capping at temperature inversions at the point of emission (run NO-CAP) and without plume injection due to plume buoyancy, i.e. emissions at stack height (run NO-RISE). Results are shown in Fig. D1. Results are generally improved in CTRL compared to NO-CAP or otherwise comparable. Results in NO-RISE are worse, with tracers generally concentrated in the lowest 100 m, and plume enhancements are overestimated compared to observations.

To evaluate model performance further, specific cases during the different meteorological situations discussed earlier are examined in more detail. They are selected to illustrate model behaviour after examination of all cases shown in Fig. 6. The first case on 30 January is during the cold stable polluted AC–C period. The second case from 8–9 February is during the Mixed period with lower surface concentrations, and the third case on 25 February is at the end of T–W when temperatures were warmer, but stable surface conditions resulted in high surface pollution levels. Results are shown in Figs. 7 and 8. Observed Helikite temperature profiles are shown together with radiosonde temperature profiles at 15:00 and 03:00 AKST for the days in question, for each case in Fig. 7a. Radiosonde profiles are shown to provide information regarding the diagnosed SBIs and EIs used in the plume rise capping parameterisation. For each case, observed plume enhancements of δNO_x and/or δCO are shown
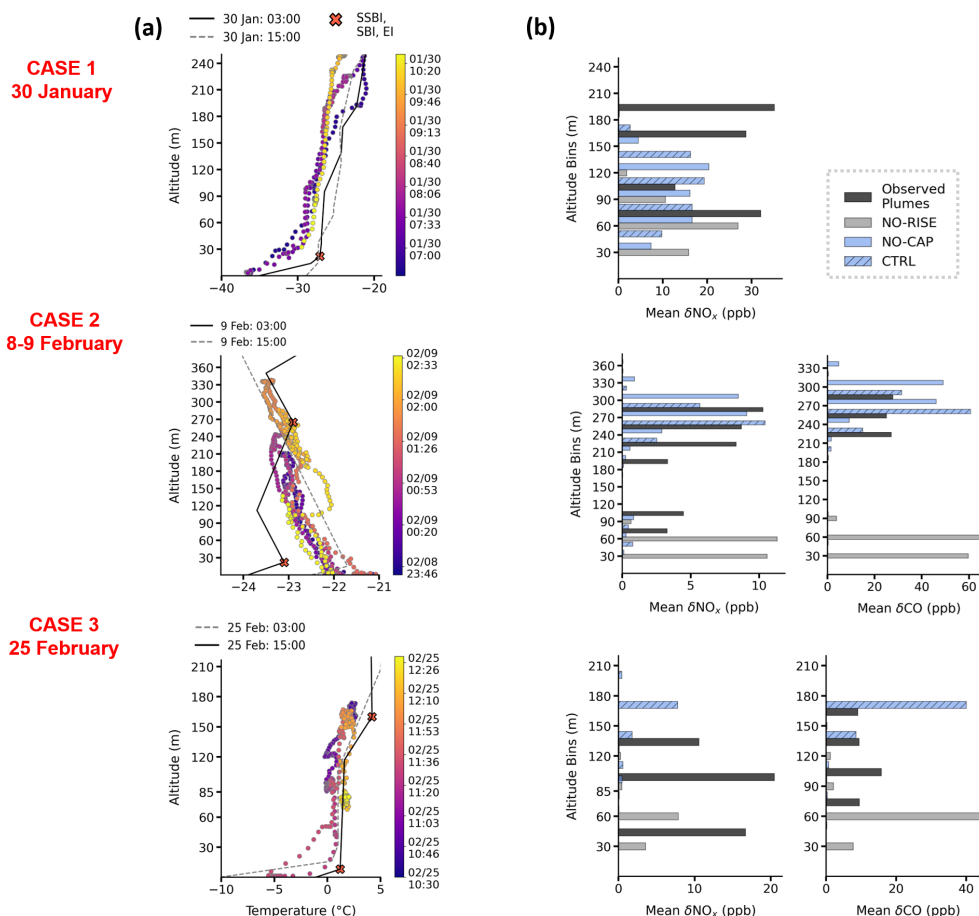
Figure 7. (a) Temperature profiles (°C) recorded during the Helikite flight for the cases highlighted in **(a)** and **(b)**. Coloured circles correspond to the time during the flight. Radiosonde temperature profiles (°C) used for the calculation of plume rise are also shown (solid black lines) and 12 h before or after the flight (dashed grey line). Derived temperature inversions (at temperature, °C; height, m) are indicated as red crosses. **(b)** Modelled (CTRL) power plant tracers compared to observations for CO and/or NO_x (ppb) averaged over altitude bins every 30 m (indicated on the y axis) at the time of the Helikite flight. For panels **(a)** and **(b)**, cases 1–3 are shown from the top to the bottom. See text for more details.

together with model results from CTRL and NO-CAP or NO-RISE. Results are binned over altitudes and averaged over the four grid cells surrounding the UAF Farm (Fig. 7b). Modelled vertical cross sections (total power plant tracer) for a period that extends several hours before and after the flight are also shown together with observed plume altitudes and concentrations (Fig. 8a). In addition, hourly power plant contributions (%) (summed over all altitudes) are provided in Fig. 8b, and the altitudes corresponding to the 95th percentile for all contributing power plants are shown in Fig. 8c, allowing identification of the origin of different plumes.

Case 1 – 30 January 2022, Fig. 7 top panels and Fig. 8 left panels. This case during AC–C is characteristic of SS surface conditions with low wind speeds ($< 1\,\mathrm{m\,s^{-1}}$) from the east or north-east ($\frac{\mathrm{d}T}{\mathrm{d}Z}$ up to 30 °C per 100 m at 0–25 m) and some stratification in the layers aloft ($\frac{\mathrm{d}T}{\mathrm{d}Z}$ up to 10 °C per 100 m, at 100–300 m; see Fig. 3e). Only NO_x observations are available for this case because of issues with the

CO sensors on 30 January. Two plumes are identified between 70–110 and 160–210 m altitude, just below elevated inversions observed in the Helikite temperature profile data (Fig. 7a). Modelled plumes are between 30–150 m and attributed predominantly to Doyon and UAF A and B. Aurora contributes most at 120–150 m, notably between 07:00 and 09:00 AKST with some downward transport to around 100 m between 09:00 and 10:30 AKST (Fig. 8a, c). The EI in the Helikite temperature profile occurs around 210 m, indicating trapping of the upper observed plume. However, no capping is applied in CTRL for the Aurora emissions because the predicted plume rise is lower than the radiosonde EI (398 m). Therefore, the calculated emission injection height for Aurora until 09:00 AKST is 150 m (midpoint) and is the same in CTRL and NO-CAP. Moreover, at 03:00 AKST on 30 January (time of radiosonde), the observed lidar wind speeds at CTC (900 m south-east of Aurora) were up to $4\,\mathrm{m\,s^{-1}}$ at the Aurora stack height (48 m), while the radiosonde wind
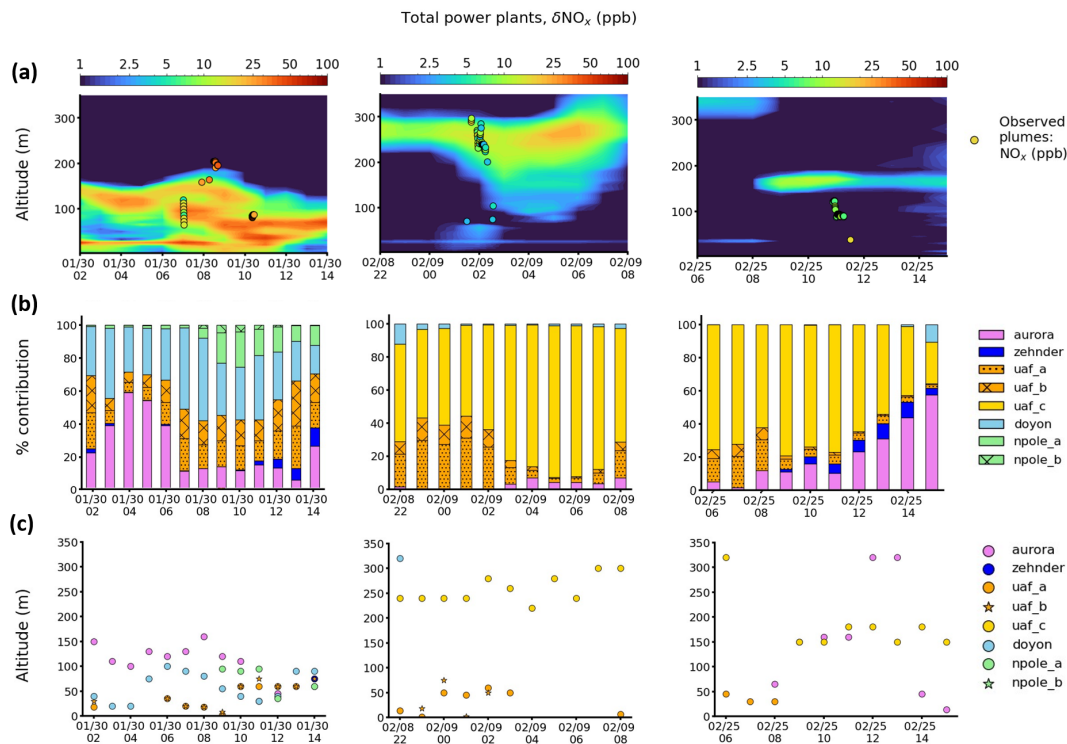
Figure 8. (a) Vertical cross section of total simulated (CTRL) power plant tracer over several hours before, during, and after each flight, with observations included as scatter points (as in Fig. 6). **(b)** Hourly percentage contributions from different power plant stacks throughout the vertical profile. **(c)** The altitude (m) where the 95th percentile of tracers resides, for each contributing power plant stack, as a function of time (hourly). For panels **(a)** to **(c)**, cases 1–3 are shown from left to right. See text for more details.

speeds were lower than $1\,\mathrm{m\,s^{-1}}$ ($>5\,\mathrm{km}$ south-west of Aurora). Since radiosonde wind speeds are used to calculate plume rise, this suggests that the simulated altitude of the Aurora plume may be underestimated due to a lack of observed spatial coverage in the parameterisation. This may also contribute to an underestimation of the plume injection height and explain why the model does not capture the observed plume at 160–210 m.

Case 2 – 8–9 February 2022, Figs. 7 and 8 middle panels. This case, during the Mixed period, contrasts to the previous SS case and is characteristic of WS conditions. Wind directions from the south to south-west transport pollution to the north (0–500 m altitude). At the time of this local nighttime Helikite flight, conditions were more stable than during the daytime, with pollution trapped at the surface due to a drop in wind speeds and an increase in SBI strength (Fig. 3). A weak EI was observed aloft at 260 m at 03:00 AKST, as shown in Fig. 7a, resulting in dispersed plumes of NO_x and CO aloft over the UAF Farm. In this case, the radiosonde-derived EI agrees with the observed Helikite EI, and, even if the stratification is rather weak, a layer of trapped emissions, with observed CO and NO_x enhancements, is evident. However, below 270 m, the radiosonde temperature profile shows an SBI, in disagreement with the Helikite profile, which has a negative temperature gradient, likely due to influence from

the drainage flow at the UAF Farm (see Appendix B and Fochesatto et al., 2024). Modelled plume enhancements from CTRL compare well with the observed plume aloft between 250–300 m with some downward transport (to 200 m) toward the end of the flight, which is also observed. This plume is attributed to UAF C. In this case, EI capping is applied and improves the modelled plume altitude compared to NO-CAP. Simulated plumes are much too low (30–60 m) in NO-RISE, highlighting the need to include plume buoyancy calculations (Fig. 7b) as shown in previous studies (e.g. Briggs, 1984; Akingunola et al., 2018). A lower-altitude plume between 50–100 m is only observed in the NO_x data. Only small enhancements (<1 ppb) are simulated in CTRL, and also in NO-CAP, and are attributed to UAF A and B stacks. They have lower stack heights and run on diesel, which may explain the lack of observed CO plume enhancements. The model may be underestimating NO_x in this case, or surface-emitted tracers may be lofted vertically and contribute to the observed plume at 50–100 m.

Case 3 – 25 February 2022, Fig. 7 lower panels and Fig. 8 right panels. This case is at the end of T–W. A plume with relatively small NO_x enhancements (<5 ppb mean δNO_x) is observed at approximately 50 m, and an elevated plume is observed with increased enhancements in NO_x between 85–120 m (5–10 ppb δNO_x) and 120–160 m in CO (25–30 ppb).

The Helikite temperatures indicate EIs near 85 and 120 m (Fig. 7a). The plume aloft, which encompasses most of the data points for both δCO and δNO_x, is captured in CTRL but not in NO-CAP. This is due to the EI observed by the 15:00 AKST radiosonde (160 m) that is used to calculate the plume injection height in CTRL, while in NO-CAP the injection altitude is approximately 500 m, demonstrating the importance of the capping parameterisation. However, the modelled plume altitude is likely overestimated by approximately 30–50 m due to the EIs occurring at lower altitudes at the UAF Farm (Fig. 7a). There is better agreement of modelled δCO with the observed enhancements than for δNO_x (Figs. 7b and 8a), which can be explained by contributions from different power plants. The UAF C stack contributes to δCO directly at the UAF Farm, as shown in Fig. D2a. UAF C, Aurora, and Zehnder contribute to modelled δNO_x (Fig. 8c), but UAF C NO_x emissions are low compared to CO because the stack has more NO_x emission controls (ADEC, 2020) (see Appendix A1). Aurora and Zehnder plumes are displaced to the south of the UAF Farm due to a displacement in modelled wind direction (north-east vs. east). This results in stronger transport to the south, displacing the simulated plumes slightly south of the UAF Farm (Fig. D2b), most likely explaining the underestimated modelled NO_x enhancement. NO_x plumes are also displaced southward in a supplementary case on 3–4 February from the Doyon power plant between 120–180 m (Fig. D2c in Appendix D1).

Appendix Fig. D3 shows Doppler wind lidar observations for cases 1 (CTC) and 2 (UAF Farm). In each case, plumes are identified by the wind lidar at a comparable altitude to the identified plumes at the farm. Although the wind lidar is sensitive to aerosols and not trace gases, it is possible that primary and secondary aerosols are contributing to observed aerosols. The results suggest that power plants are also a source of aerosol over Fairbanks (more details in Appendix D2).

Overall, based on the evaluation of these cases, the CTRL run, including plume rise and capping using information on the ABL structure, often performs best compared to available profile observations. Therefore, CTRL is used in the following examination of processes influencing surface pollution during ALPACA-2022. Evidently, plume rise and capping have to be taken into account, but, ideally, using vertical profile information at the point of injection would be required to improve the plume rise calculations. Discrepancies in modelled winds sometimes lead to displacement in modelled plumes, as shown by case 3 and the supplementary case on 3–4 February (Appendix D1). This is important for power plant facilities located away from the UAF Farm, e.g. Aurora and Doyon.

6   Processes influencing simulated surface trace gases

Model results from the CTRL run are initially evaluated against surface observations. To understand model behaviour during different meteorological conditions and to examine possible causes of model discrepancies, the sensitivity of model results to various processes is then explored (shown in Table 4). This analysis is not exhaustive in terms of the processes considered, and other possible processes are highlighted in the discussion of the results.

6.1   Evaluation against surface observations

Total modelled CO, SO_2, and NO_x from surface-emitted and power plant sources in the surface layer between 0–5 m compared to available surface observations as a function of time, Downtown, are shown in Fig. 9a. Note that SO_2 results include wet and dry deposition, but their influence is small as noted earlier (also Appendix E3). Downtown observations correspond to CTC and NC data averaged for CO and SO_2 and compared with the closest grid cell to the Downtown area, while NO_x observations are only available at the CTC site. Diurnal cycles of the observations and model results during the entire campaign (all data) and events AC–C, T–C, Mixed, and T–W are shown in Fig. 9b. Results for the HA site in eastern residential Fairbanks and the UAF Farm are provided in Figs. E1 and E2. Normalised mean biases (NMBs) and normalised mean errors (NMEs) for Downtown using hourly results are provided in Table 5. Both metrics are shown as fractions with no units, and equations are given in Appendix E1. Tables E1 and E2 correspond to HA and the UAF Farm in Appendix E2.

As discussed earlier, observed CO, SO_2, and NO_x are enhanced during stable conditions. Observed variability with larger concentrations in SS compared to WS conditions is generally captured. CO concentrations and variability are simulated reasonably well. However, while the NMB is 0.02 over the entire campaign (all data), the NME is 0.52 (Table 5). There are also negative biases during the stable transient events T–C and T–W (NMBs = −0.34 and −0.55) and a strong positive bias during the Mixed period (NMB = +0.5). Since CO has a long photochemical lifetime in winter of the order of months, discrepancies may be caused by meteorology.

SO_2 and NO_x tracer variability in CTRL is comparable to that of CO. However, for SO_2 there are large overestimates, in particular during the Mixed period (NMB = +1.26, NME = 1.37, Table 5). The main source of SO_2 in Downtown Fairbanks is residential distillate oil in the space heating sector emissions (Fig. A1). This source is released up to 12 m, with 85 % of the emissions released above 5 m. Therefore, these emissions can be transported to the surface and higher in altitude. Modelled SO_2 appears to be sensitive to the vertical transport of these emissions and is explored in

Table 4. Surface sensitivity simulations. See text for details.

Sensitivity simulation	Tracer	Description
CONST-EM	CO SO$_2$ NO$_x$	CTRL with constant emissions
NOx_Emissions	NO$_x$	CTRL + temperature-dependent diesel vehicle emissions
NOx_Emissions_LT		NOx_Emissions + variable photochemical lifetime
SO2_SOR	SO$_2$	SO2_CTRL + sensitivity to oxidation ratio
MixH_100_CO	CO	CTRL + $h_{\min} = 100\,\mathrm{m}$
MixH_100_SO2	SO$_2$	SO2_SOR + $h_{\min} = 100\,\mathrm{m}$
MixH_100_NOx	NO$_x$	NOx_Emissions_LT + $h_{\min} = 100\,\mathrm{m}$
MixH_10_CO	CO	CTRL + $h_{\min} = 10\,\mathrm{m}$
MixH_10_SO2	SO$_2$	SO2_SOR + $h_{\min} = 10\,\mathrm{m}$
MixH_10_NOx	NO$_x$	NOx_Emissions_LT + $h_{\min} = 10\,\mathrm{m}$

the sensitivity analysis. Although the photochemical loss of SO$_2$ by OH is not considered to be important during the winter (e.g. Green et al., 2019), oxidation by other reactions may be important. In contrast, the model significantly underestimates observed NO$_x$, especially in SS conditions (NMB $= -0.65$ and -0.8, events AC–C and T–C with comparable NMEs, Table 5). Moreover, an overestimate might be expected because the lifetime of NO$_x$ is not included in CTRL. The sensitivities of modelled SO$_2$ and NO$_x$ to processes governing their lifetimes are considered in Appendix E5.

Observations at HA in the east residential area of Fairbanks follow the same general variability as the Downtown area but differ during the strongly stable events AC–C, T–C, and T–W, as highlighted by the diurnal variations (Figs. 9b and E1b). The Downtown sites are located close to main roads, leading to higher observed NO$_x$ mixing ratios than at the HA site. CO magnitudes are more comparable because of higher contributions from residential wood burning at the HA site, as supported by the strong peak around 06:00 AKST in the diurnal cycle of CO at HA (Fig. E1b). However, Downtown, the diurnal cycle follows the on-road mobile sector (Fig. 9b). The agreement between model and observations is weaker at HA; for instance the NME is 0.56 (Table E1) in contrast to 0.37 Downtown (Table 4) for CTRL_CO because the horizontal resolution of the surface emissions (1.33 km grid spacing) may be too coarse to sufficiently capture small spatial differences within the city. Emission source contributions for CO and NO$_x$ in the Downtown and HA areas are comparable (Fig. A1), supporting this argument. It should also be noted that the model results shown in Fig. 9 are interpolated onto the same grid as the emissions (1.33 km). Furthermore, the locations of meteorological data assimilated in EPA-WRF are biased toward the Downtown area, potentially leading to more realistic simulated meteorology. Moreover, during SS conditions, horizontal transport is hindered in Fairbanks, leading to a large variability in the observations at different locations. This was demonstrated by Robinson et al. (2023) during multiple mobile sniffer drives of PM$_{2.5}$ around Fairbanks.

At the UAF Farm site, smaller surface CO mixing ratios are observed. Over the entire campaign, NMBs and NMEs are comparable to those Downtown, but biases are higher when stable conditions influence the Downtown area more than the UAF Farm, especially during the AC–C period. A local flow that originates from large-scale north-easterly winds intermittently descends into the Goldstream Valley to the north-west, resulting in a dominant north-westerly flow at the UAF Farm toward the surface (Maillard et al., 2022; Fochesatto et al., 2024). The wind direction of the local flow is captured by EPA-WRF at 10 m due to data assimilation. However, underestimations in horizontal wind speeds can occur when strong static stability is observed (strong temperature gradients) due to difficulties in simulating dynamic instability (turbulence and/or wind shear) induced by the local flow (e.g. Fig. B2 during AC–C).

6.2 Sensitivity simulations

Following the initial evaluation, the sensitivity of modelled tracers to meteorology, emissions, and vertical mixing is explored. A description of the sensitivity to NO$_x$ trace gas lifetimes is included in Appendix E5. The series of sensitivity simulations, carried out to better understand processes influencing modelled surface tracers and which may help explain model biases, are summarised in Table 4.

6.2.1 Sensitivity to meteorology

As noted earlier, model biases can be induced by errors in EPA-WRF or treatments in FLEXPART-WRF of vertical or horizontal transport. Of particular interest are discrepancies during cold stable periods with poor air quality. For example, the NMB and NME of CO during T–C are -0.34 and 0.39, respectively. Temperature gradients at CTC (dT 23–3 m) are
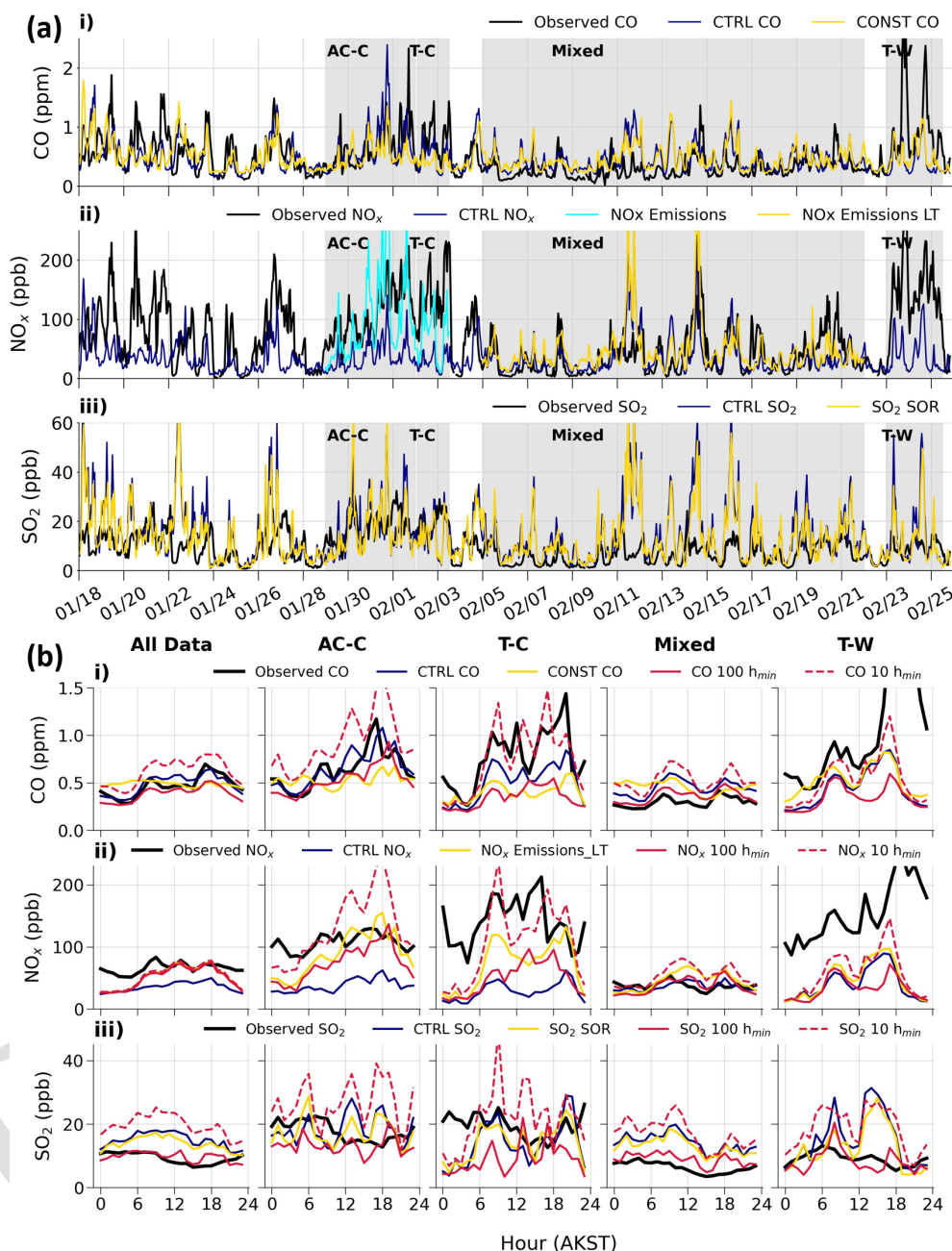
Figure 9. (a) Total modelled surface and power plant tracers (in ppb) as a function of time between 0–5 m for CTRL and selected sensitivity simulations described in Table 2 compared to available surface observations Downtown for (i) CO, (ii) NO$_x$, and (iii) SO$_2$. **(b)** Diurnal cycles, Downtown, for observations (black) and model simulations (colours as in **a**), averaged over all data (left) and over events AC–C CE10, T–C, Mixed, and T–W. CONST CO signifies the CONST-EM sensitivity run. CE11

generally well captured by EPA-WRF since the model is nudged with these temperatures. However, dT 23–3 m is not well reproduced in EPA-WRF during T–C on 2–3 February when the very large observed dT (up to 8 °C) is underestimated by 3 °C (Fig. B1b). The 23 m CE12 wind speeds measured at CTC are also overestimated, resulting in stronger horizontal transport at the surface compared to observations (Fig. B1). There is also more upward vertical transport of

tracers on 1 February (Fig. 5). Consequentially, modelled CO is underestimated during T–C. This could be explained by a transient synoptic condition (i.e. a low-pressure weather system) in upper layers above the surface layer from 2–3 February (T–C), disrupting the vertical stratification provided by the stable anticyclonic conditions that occurred from 29 January to 1 February (AC–C). Yet, at the surface, local-scale radiative cooling persisted, and strong temperature gradi-

Table 5. Normalised mean biases (NMBs) and normalised mean errors (NMEs) of model simulations (total tracers) at the surface Downtown compared to surface observations Downtown (CTC and NC averaged), at hourly time resolution. NMBs and NMEs are given for all data and the meteorological events AC–C, T–C, Mixed, and T–W. Bold and italic fonts correspond to the smallest and largest NMBs and NMEs, respectively, for each period and each tracer.

Simulation name	NMB					NME				
	All data	AC–C	T–C	Mixed	T–W	All data	AC–C	T–C	Mixed	T–W
CTRL CO	**0.02**	**0.02**	−0.34	0.5	−0.55	0.52	0.39	0.37	0.68	0.56
CONST-EM CO	0.03	−0.17	−0.46	0.54	**−0.45**	0.54	0.37	0.5	0.73	**0.5**
MixH_100_CO	*−0.19*	−0.17	*−0.55*	**0.21**	−0.64	**0.47**	**0.34**	*0.55*	**0.48**	*0.64*
MixH_10_CO	0.3	*0.45*	**−0.04**	*0.79*	−0.45	*0.66*	*0.66*	**0.35**	*0.92*	0.51
CTRL NO$_x$	*−0.46*	*−0.65*	*−0.8*	−0.03	−0.74	*0.69*	*0.66*	*0.8*	0.66	0.74
NOx_Emissions	**−0.07**	**−0.05**	−0.47	*0.59*	−0.67	0.68	0.45	0.5	*0.93*	0.67
NOx_Emissions_LT	−0.23	−0.17	−0.5	−0.21	0.7	0.61	**0.41**	0.52	0.7	0.7
MixH_100_NOx	−0.25	−0.32	−0.67	**−0.01**	*−0.77*	0.61	0.42	0.67	**0.65**	*0.77*
MixH_10_NOx	−0.2	0.2	**−0.25**	0.44	**−0.62**	**0.61**	0.53	**0.44**	0.76	**0.62**
CTRL SO$_2$	0.6	0.03	−0.3	1.26	0.6	0.94	0.49	0.4	1.37	0.95
SO2_SOR	0.47	**−0.02**	−0.29	1.08	0.32	0.84	0.48	**0.37**	1.22	0.74
MixH_100_SO2	**0.03**	−0.26	*−0.57*	**0.43**	**−0.08**	**0.62**	**0.42**	*0.63*	**0.7**	**0.54**
MixH_10_SO2	*1.08*	*0.5*	**0.1**	*1.71*	*1.0*	*1.31*	*0.79*	0.55	*1.8*	*1.18*

ents were maintained and strengthened due to the arrival of the warm air mass aloft, as also observed by Mayfield and Fochesatto (2013).

During the warm polluted period T–W at the end of the campaign (23–25 February) under AC to cyclonic transient conditions, CO and NO$_x$ are underestimated compared to observations. This was an unusual event during which the SBI was very strong, but temperatures were warmer (-10 to $5\,°C$) than in AC–C and T–C, for example. While observed temperature gradients at CTC are captured well by EPA-WRF during this period, horizontal transport appears to be overestimated because the EPA-WRF wind speeds are slightly higher than observations close to the surface, e.g. at 10 m (Fig. B1). This may partly explain the low model NMB during this period (CO $= -0.55$ and NO$_x = -0.74$, respectively; Table 4). During the Mixed period, the dT (23–3 m) is often too high compared to observations, for example on 16 February (Fig. B1). This leads to overestimates in modelled mixing ratios, in particular for SO$_2$ (Fig. 9).

In order to explore the influence of meteorological variability on simulated tracers at the surface, the model is run with constant emissions (run CONST-EM; see Fig. 9a). For this run, hourly emissions are averaged over the full campaign, removing the diurnal and weekday/weekend variability and the effects of temperature on the emissions. Results are examined for CO since, due to its long photochemical lifetime in winter, simulated CO is only dependent on meteorology; i.e. it has no chemical loss. Note that NO$_x$ and SO$_2$ with constant emissions were also simulated (not shown) and are more comparable to the CTRL simulation. Differences in diurnal cycles for CTRL and CONST-EM CO are also shown in Fig. 9b. In general, CONST-EM CO shows the same variability over time as CTRL. For example, CONST-EM CO

is higher during the stable polluted AC–C period compared to the less stable Mixed period (Fig. 9a, b). CONST-EM results also exhibit some diurnal variability, albeit less than in CTRL and compared to the observations. These results highlight that variations in meteorological conditions, including diurnal effects, are an important factor controlling pollutants at the surface. Differences between CONST-EM and CTRL also show the importance of diurnal variations in CO emissions during pollution episodes. Surface CO emissions are dominated by the on-road sector Downtown (see Fig. A1). Nevertheless, the CONST-EM negative biases are more pronounced in cold polluted periods than in the full campaign, showing the cold-temperature dependence of CO petrol emissions is important. In summary, CO biases can be explained partly by emission variability and by differences in modelled and observed meteorology influencing tracer transport and mixing, as well as ABL stability. Discrepancies due to meteorology are linked to the EPA-WRF simulation, as discussed above, and also to treatments of vertical mixing and turbulence in FLEXPART-WRF. The sensitivity of results to the mixing height parameter in the FLEXPART-WRF BL scheme is examined further in Sect. 6.2.4.

6.2.2 Sensitivity to vehicle NO$_x$ emissions at cold temperatures

The underestimation of NO$_x$ during SS periods, such as AC–C, is more significant than CO and SO$_2$ and may indicate a missing source of NO$_x$. The on-road sector is an important source of NO$_x$ in the Downtown area (Fig. A1), in which diesel is the largest contributor, even if the fraction of diesel vehicles is rather low (9 % diesel versus 90 % petrol vehicles in Fairbanks non-attainment area, US EPA 2022). The
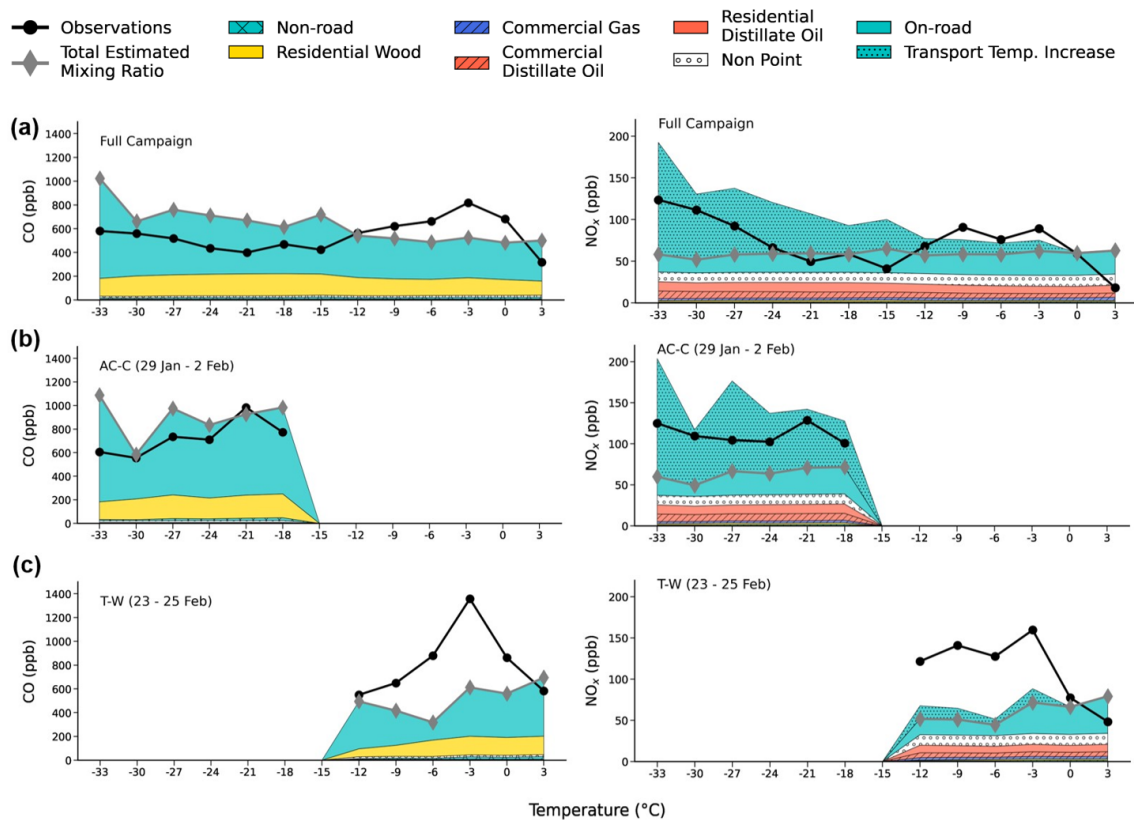
Figure 10. Estimated mixing ratios in ppb based on ADEC surface emission fluxes and a 10 m mixing depth, averaged over the Downtown area, compared to observed mixing ratios in ppb at the CTC site (black circles), averaged over 3 °C temperature bins for **(a)** the full campaign, **(b)** 29 January to 2 February, and **(c)** 23 to 25 February for CO (left) and NO_x (right). The shaded colours correspond to the contributing emission sectors indicated in the legend (total of all sectors – grey diamonds). The mid-point of the 3 °C temperature bin is shown on the x axis. The increment in NO_x vehicle emissions at low temperatures, according to the log-linear temperature dependence, is also shown with cyan shading and dotted hatching. See text for details.

diesel fleet in the area is predominantly made up of heavy-duty trucks. In 2022, US EPA used the MOtor Vehicle Emission Simulator 3 (MOVES3) (U.S. EPA, 2021) to calculate on-road emissions, which were subsequently processed with the SMOKE model. MOVES3 includes a higher incremental temperature dependence of CO compared to NO_x petrol emissions, which is important because CO emissions are much higher than NO_x emissions for petrol. In addition, cold-temperature dependencies for diesel vehicle cold starts for both CO and NO_x are set to zero; however, data were only collected down to +1.5 °C in that study (U.S. EPA, 2015). More details are provided in Appendix E4. Several studies have shown that NO_x emissions from diesel vehicles are higher at cold temperatures, in particular in modern vehicles with selective catalyst reduction (SCR) units that have been introduced following more stringent emission regulations. Failure to heat the diesel exhaust fluid (DEF) injection to the required temperature to initiate the SCR units is considered to contribute to enhanced emissions (Weber et al., 2019; Selleri et al., 2022; Seo et al., 2022; Wærsted et al., 2022). Ambient temperatures in Fairbanks reach −40 °C, up

to 25 °C lower than the lowest temperatures examined in these studies. Hence, the lack of cold-temperature dependence for diesel NO_x emissions in MOVES3 may be contributing to the substantial underestimation of modelled NO_x during cold conditions. Other emission inventories, such as CAMS, also have a weaker temperature dependence for NO_x vehicle emissions than CO at low temperatures (Guevara et al., 2021). This may be because current emission inventories are based on older vehicles without SCR units, which are associated with newer diesel vehicles, or due to limited research on this topic in very cold environments.

The possible contribution of temperature-dependent diesel emissions to CO and NO_x concentrations in Fairbanks is investigated based on the ADEC surface emission fluxes that are used in the model simulations. In order to compare to surface observations at CTC, surface fluxes for each emission sector, in $kg\,m^{-2}\,s^{-1}$, are converted into hourly mixing ratios (in ppb) by taking into account the volume of each emission grid cell (1.33 km^2 × 10 m (AGL) in vertical). These estimates are averaged over the four grid cells covering the Downtown area. The results are shown in Fig. 10

averaged over 3 °C temperature bins over the full campaign, the cold polluted period (AC–C, 29 January to 2 February), and the warm polluted period (T–W, 24 to 25 February). At intermediate temperatures (−13 to −23 °C), common during the Mixed period, estimated NO_x mixing ratios are overestimated compared to observations. This is in part because meteorology and mixing are not considered, as also shown for CO. However, the observations show a clear increase in NO_x at colder temperatures, especially below −23 °C, which is much less distinct for observed CO. For CO, as noted earlier, a cold-temperature dependence is already included for mobile (on-road and off-road) petrol emissions in MOVES3, and there is better agreement between the CO observations and estimated mixing ratios during AC–C (Fig. 10b). The poor agreement between NO_x observations and estimated NO_x during AC–C supports the hypothesis that an increase in diesel NO_x vehicle emissions due to a cold-temperature dependence may be required. Furthermore, estimated CO and NO_x mixing ratios are both underestimated during T–W (Fig. 10c), indicating that a cold-temperature effect is not driving the discrepancy in this period.

Temperature-dependent NO_x emissions are revisited based on a study of diesel vehicles in Norway that found a factor of 3 increase was required at −13 °C with a linear increment from 2.9 to 1.0 between −13 and +14 °C, respectively (Wærsted et al., 2022). Here, emission enhancements for total mobile emissions using a log-linear function from a factor of 1.5 to a factor of 10 are calculated for daily average temperatures (at CTC) between 0 and −40 °C. For example, the increment is ×3 at −20 °C and a factor of 6 at −30 °C (see Fig. E3). A log-linear function is also used in MOVES3 for the temperature-dependent increase in petrol emissions (U.S. EPA, 2015). Estimated mixing ratios including the cold-temperature dependence are also shown in Fig. 10. Inclusion of this NO_x emission enhancement significantly reduces discrepancies compared with observations during AC–C with very cold temperatures, and biases for the cold and warm polluted events are now comparable to CO (Fig. 10). However, observed NO_x at intermediate temperatures between −22 and −13 °C is now overestimated. This corresponds to temperatures during the Mixed period when surface conditions varied between SS and WS conditions, and the discrepancy between observed and estimated CO and NO_x is expected to be influenced more by meteorology and BL stability, as discussed previously.

The log-linear NO_x temperature dependence is applied to modelled mobile emissions tracers in the NOx_Emissions run, leading to significant improvements compared to the observations (see Fig. 9), especially during cold stable conditions; e.g. the NME is reduced from 0.8 to 0.5 during T–C. The results suggest an increase in NO_x emissions from diesel vehicles is needed during periods with very cold temperatures, in particular below −20 °C. The modelled NO_x diurnal cycle also shows a clear improvement during the daytime, although differences compared to the observations remain at nighttime. This can be partly explained by difficulties in modelling extremely stable conditions that are enhanced at nighttime. For example, during T–C, there is also an underestimation of CO and SO_2 between 00:00 and 06:00 AKST. However, the large nighttime underestimation of NO_x with respect to CO (e.g. for all data) may indicate an underestimation of NO_x from residential distillate oil emissions (Fig. A1). These emissions dominate at night when mobile emissions are low and warrants investigation in future studies. In event T–W, the bias reduction is small, and the NMB remains strongly negative at −0.67 because only a small increment is applied to the mobile NO_x emissions at warmer ambient temperatures. The fact that both CO and NO_x are underestimated during this period suggests that these biases are unlikely to be due to the cold-temperature dependence but potentially due to uncertainty in the mobile emissions on these days and/or overestimated horizontal transport induced by modelled surface stability, as discussed in the previous section.

Discrepancies in modelled NO_x could also be explained by inclusion of atmospheric lifetimes and is explored in Appendix E5 (run NOx_Emissions_LT, shown in Fig. 9 for the Mixed period). Notably, inclusion of a shorter atmospheric lifetime during WS conditions improves agreement compared to observations during the Mixed period because O_3 transported from aloft leads to titration of NO by reaction with O_3 (NME is reduced from 0.93 to 0.7). This has a minor effect during SS conditions when a longer lifetime is expected due to O_3 titration by excess NO and limited O_3 production or transport from aloft. However, assumptions about NO_x lifetimes in this study are simple, and a more sophisticated investigation into NO_x chemical processing may be required moving forward.

6.2.3 Sensitivity to SO_2 oxidation

Dry and wet deposition is included in the CTRL SO_2 simulation, and a photochemical lifetime is not considered because it is too long during Arctic wintertime (Yu et al., 2018; Green et al., 2019) (Appendix E5). Appendix E3 explains the impacts of deposition on SO_2. However, SO_2 can be oxidised and forms secondary sulfate species through other reactions, e.g. by oxidation with hydrogen peroxide (H_2O_2) (Alexander et al., 2012; Moon et al., 2023a). Based on isotope observations used in Moon et al. (2023a), it is shown that secondary sulfate aerosol formation increased in February (average 44.4 % secondary sulfate) compared to January (average 27.5 % secondary sulfate) during ALPACA-2022, consistent with the higher observed sulfur oxidation ratio (SOR), an indicator of secondary aerosol formation. Increased secondary sulfate formation in February was due to more WS conditions with higher O_3 concentrations at the surface, higher humidity, and more clouds, promoting oxidation through aqueous and heterogeneous chemistry.

Here, the SO2_SOR sensitivity explores an effective reduction in SO_2 by reducing SO_2 emissions using daily SOR values calculated in Moon et al. (2023a) (Table 4). Modelled SO_2 overestimates are reduced for the entire campaign and, notably, in late February as discussed earlier (NMEs were reduced from 0.94 to 0.84 during the entire campaign and from 0.95 to 0.74 during T–W). The remaining overestimates during T–W may be due to residential heating emissions being too high during the warm polluted period. However, since a temperature dependence has already been applied in the residential heating emissions, this is unlikely to be the controlling factor. Another possible reason could be that SO_2 oxidation was enhanced due to the presence of aerosol haze that occurred during this period. Such pollution haze has previously been shown to promote oxidation of SO_2 (e.g. Wang et al., 2014). Overestimation of SO_2 may also be influenced by modelled vertical mixing and is explored in the following section.

6.2.4 Sensitivity to vertical mixing

In a final set of sensitivities, vertical mixing near the surface is explored. Results of these simulations are included in Fig. 9b showing diurnal cycles. More details about the model setup and interpretation of the results are provided in Appendix E6. A mixing height of 20 m (CTRL) is optimal for CO and NO_x tracers (all data). However, during periods of increased stratification (strong SBIs or SSBIs), including T–C and T–W, inhibited vertical mixing is better simulated when $h_{min} = 10$ m. On the other hand, runs with $h_{min} = 100$ m improve simulated tracer concentrations during WS conditions with enhanced vertical transport. SO_2 is more complex because space heating emissions are mainly emitted above the surface (5–18 m), and $h_{min} = 100$ m better represents vertical mixing of the tracers above the surface. The exception is during T–C, when $h_{min} = 20$ m performs better. Overall, the results suggest improvements are needed to the treatment of vertical mixing in FLEXPART-WRF during wintertime Arctic conditions. However, we note that SO_2 overestimates may also be influenced by additional chemical processing not accounted for in Sect. 6.2.3 or by underestimation of dry or wet deposition. Variable results among pollutants could also indicate compensating errors in the model.

7 Conclusions and future perspectives

This study presents a detailed investigation of processes influencing wintertime pollution from surface urban and elevated point sources in Fairbanks, a sub-Arctic city in Alaska, exploiting Lagrangian particle dispersion modelling and comprehensive surface and vertical profile measurements made during the ALPACA campaign in January–February 2022 (Simpson et al., 2024). To evaluate the dispersion and vertical distribution of different pollution sources in the Fairbanks area, high-temporal- and high-

spatial-resolution surface and power plant emission tracers of CO, SO_2, NO, and NO_2 have been included in the FLEXPART-WRF model. To account for the presence of stable layers at the surface and aloft, a scheme for estimating power plant emission injection heights in FLEXPART-WRF was implemented using detailed information about the power plant stack emissions, building on the previous work of Briggs (1984) in stable conditions. Comparison of simulated tracer distributions with observations and sensitivities to switching off power plant plume rise and plume capping in stable layers show that accounting for plume buoyancy and capping emission injection is critically important for accurate simulation of power plant plume injection heights and their transport downwind. In particular, the use of detailed stack parameters (stack height and radius, flue gas exit temperature, and velocity) and temperature profile measurements to diagnose the presence of inversions that trap pollution plumes is required.

Model results were evaluated depending on different meteorological conditions. Notably, analysis of surface temperature gradients identified strongly stable (SS) and weakly stable (WS) conditions close to the surface, following Maillard et al. (2022) and Simpson et al. (2024). Simulated trace gas concentrations, which are enhancements above background, emitted from surface and elevated sources, including the power plants, are larger during SS compared to WS conditions over the Fairbanks area. Vertical transport is more limited in SS conditions and by the presence of elevated inversion layers. During WS conditions, near-surface pollution is reduced, and pollution concentrations above 200 m are enhanced, owing to stronger horizontal and vertical transport, likely due to enhanced turbulent mixing. Pollution outflow to the south-west, due to dominating north-easterly winds up to 200 m, suggests a possible regional influence due to anthropogenic emissions from Fairbanks and North Pole, which requires further investigation, including exploration of recirculation. Modelled tracer concentrations are larger than those typically found in wintertime Arctic haze.

Pollution plumes observed by the Helikite aloft are generally well simulated in terms of timing and vertical distributions. These plumes are attributed to particular power plant stacks following transport by north-easterly or easterly winds to the UAF Farm site in the west of Fairbanks. In some cases, small discrepancies in EPA-WRF winds, used to drive the tracer simulations, result in displacement of the plumes, for example to the south of the measurement location. The plume rise calculations could be improved further by using WRF temperatures and winds at the location of the power plant stacks, rather than using radiosondes at Fairbanks airport, allowing spatial differences to be better captured. The treatment of vertical plume rise could be further improved by taking into account the changes in the buoyancy force of the plume as it rises above the stack, for example, as in Akingunola et al. (2018). Acquisition of more vertical pro-

file observations (e.g. using drones) at and downwind of the power plant stacks would also be valuable.

At the surface, modelled CO compares well to observations in downtown Fairbanks, with variability driven by changes in surface stability. Discrepancies are mostly explained by differences in modelled meteorology or ABL stability on short timescales. Agreement at other sites is less good. At the Hamilton Acres site in the eastern residential area, model discrepancies could be explained by the horizontal resolution of the emissions (1.33 km) being too coarse to capture the larger residential wood burning emissions at this site. Surface pollution is lower at the UAF Farm in western Fairbanks, a site also influenced by a local valley flow that frequently occurs during anticyclonic conditions, induces turbulence, and clears out surface pollution. This flow is underestimated by EPA-WRF in situations when strong static surface stability is observed and thus in the tracer simulations. This is due to misrepresentation of dynamic instability (turbulence and/or wind shear) induced by the local flow in the WRF simulations. These results highlight the complexities of dispersion modelling in a region influenced by strongly stable ABL conditions and local-scale phenomena linked to orography. Improvements to WRF simulations based on Maillard et al. (2022), who examined surface effects of the local valley flow at the UAF Farm site, or using higher-resolution model simulations, such as large-eddy simulations, may also improve results.

In contrast to CO, surface NO_x is significantly underestimated in the CTRL simulation, especially in very cold, stable conditions. A possible cause is underestimation of NO_x emissions from diesel vehicles, already shown to be important down to $-13\,°C$ (e.g. Wærsted et al., 2022). Inclusion of a log-linear temperature dependence for NO_x emissions from the mobile (on-road and off-road) sector by a factor of $×1.5$ at $0\,°C$ to $×6$ at $-30\,°C$ (average daily temperatures) considerably improves the model results (during daytime). Previous studies have not considered such large increases at very low temperatures below $-15\,°C$, warranting further investigation. Such dependencies may be due to inefficient or even failure of selective catalytic reduction units implemented in vehicles to reduce NO_x emissions (Seo et al., 2022) and should be considered in emission inventories in cold wintertime environments similar to Fairbanks. Inclusion of photochemical lifetimes for NO and NO_2 also improves simulated surface NO_x, especially during WS conditions, when O_3 concentrations are higher. Future work investigating chemical processing of NO_x and O_3 at the surface and in power plant plumes will help to better constrain NO_x lifetimes in the polluted Arctic wintertime.

Surface SO_2 is generally overestimated, despite the inclusion of simplified treatments of wet and dry deposition and an estimation of the fraction of SO_2 converted to secondary sulfate species. Discrepancies appear to be mostly driven by the vertical transport of space heating emissions, which are distributed between 5 and 18 m in the EPA-ALPACA emission inventory. This is explored by varying the minimum mixing height (h_{min}) in FLEXPART-WRF, which, in this study, influences the altitude at which surface tracers are mixed vertically. Increasing h_{min} from 20 to 100 m improves the comparison to observed SO_2 at the surface due to enhanced vertical transport of the space heating emissions. In contrast, the on-road mobile sector dominates surface emissions of CO and NO_x in central Fairbanks, and they are often trapped near the surface by very shallow SBIs or SSBIs. For these tracers, runs with h_{min} equal to 10 m limit vertical mixing and lead to further improvement in the model results compared to surface observations. Model sensitivity to the h_{min} parameter suggests that improvements are needed in the treatment of turbulent mixing during wintertime conditions with very stable boundary layers.

Overall, the findings of this study illustrate the complexity of simulating surface and elevated pollution sources in cold stable Arctic wintertime conditions. The tracer simulations, while simplified in some aspects, provide important insights into possible processes affecting trace gas pollution at the surface and aloft in the boundary layer. They form a basis for regional 3D chemical and aerosol modelling of pollution due to anthropogenic emissions over the Fairbanks region and its potential contribution to background Arctic haze during winter–spring. As the Arctic becomes more developed in the future, due to increasing human activity and climate warming, higher energy demands in Arctic communities are expected. This may lead to increases in poor air quality during Arctic winter, in particular if poor energy infrastructure persists. This study informs the policy for more stringent emission standards for surface and elevated sources, as well as an accelerated transition towards renewable energies in the Arctic region. `CE13`

Appendix A: Emissions

In this section, additional figures related to the emissions used in this study are provided. Appendix A1 provides details on emission controls used for the power plant stacks running during ALPACA-2022. Figure A1 shows campaign-averaged surface emissions for each sector in the non-attainment, Downtown, Hamilton Acres (HA), and UAF Farm areas. In the Fairbanks non-attainment area, airport emissions are large for SO_2. The emission contributions at the east residential and Downtown sites are comparable, but magnitudes are greater Downtown (Fig. A1c, d). The UAF Farm site is dominated by the mobile sector, but the magnitudes of emissions are small compared to the other locations. Figure A2 shows a time series of power plant emission data for each power plant stack for the trace gases (CO, SO_2, NO, and NO_2). Differences in trace gas emissions according to fuel type are evident in Fig. A2. For example, North Pole A emits large NO_2 emissions due to running on naphtha fuel, while NO_x and SO_2 emissions from UAF C are small compared to the other

coal-fired stacks (Aurora and Doyon), owing to more strin-
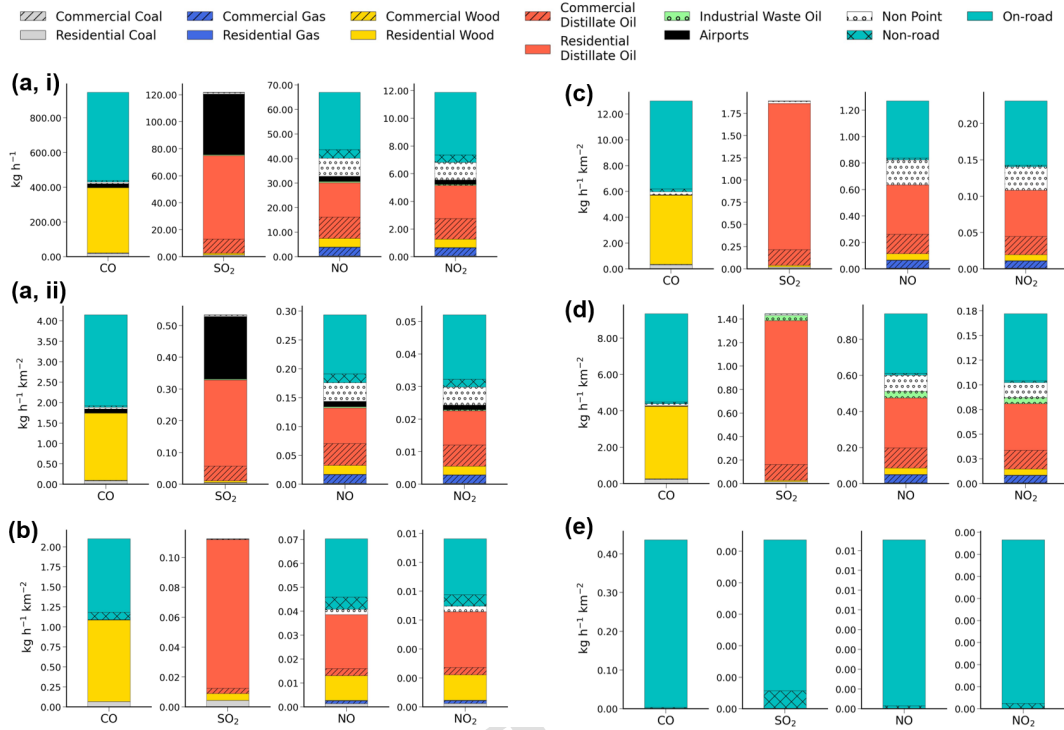gent emission controls (Appendix A1).

Figure A1. CO, SO_2, NO, and NO_2 emissions averaged over the campaign, summed between 0–18 m altitude in (**ai**) the Fairbanks non-attainment area, with a sum of 129 grid cells (1.33×133 km^2) (kg h^{-1}). In panels (**aii**) and (**b–e**), the emissions are averaged per grid cell (kg h^{-1} km^{-2}) for (**aii**) the Fairbanks non-attainment area, (**b**) the North Pole non-attainment area, (**c**) the Downtown area, (**d**) Hamilton Acres, and (**e**) the UAF Farm. Panels (**c**) to (**e**) are for the ADEC emissions grid cell closest to the location. See Fig. 1 for details.
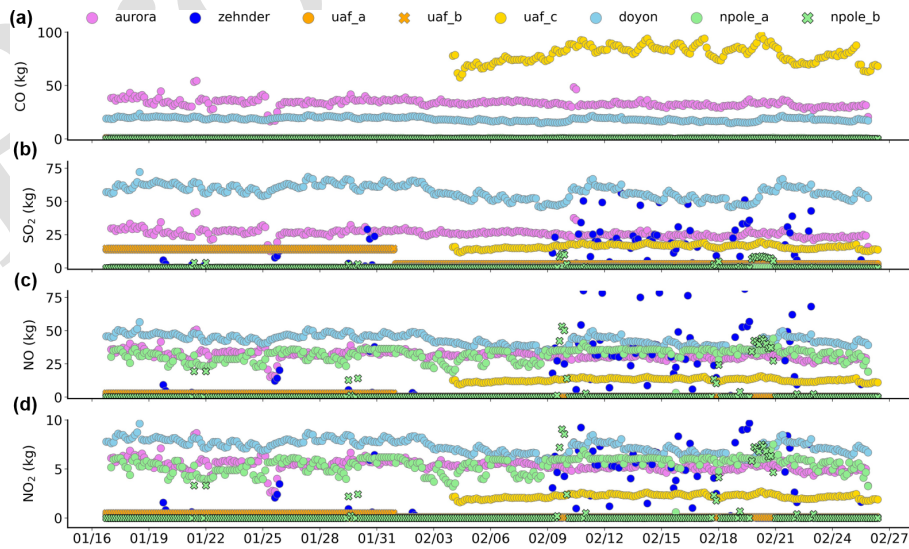
Figure A2. Emissions of (**a**) CO, (**b**) SO_2, (**c**) NO, and (**d**) NO_2 (kg) for each power plant stack (indicated above panel **a**) as a function of time during ALPACA-2022. Averages of 3 h are shown for clarification of the data points, but 1 h data are used in the modelling study.

A1 Power plant emissions control strategies

The power plant emissions used in this study were provided by each of the power plant facilities for the campaign period. The emissions vary depending on fuel type and emission reduction controls (ADEC, 2020). The UAF C coal stack uses low-NO_x burners (40 %–60 % efficiency) and staged combustion to reduce NO_x emissions. However, Aurora and Doyon (also coal) do not have NO_x emission controls such as selective catalyst reduction (SCR) units. Diesel or fuel oil power plants (Zehnder, UAF A, UAF B, and North Pole A) do not have NO_x emission reduction strategies. SO_2 control strategies include 0.25 % sulfur by weight for each coal power plant, and UAF C also uses limestone injection. North Pole A uses 20 TS3 parts per million (ppm) sulfur, while UAF A, UAF B, and North Pole B are limited to 15 ppm sulfur. The limit is as high as 1000 ppm sulfur for Zehnder, but operations are limited to $< 70\,\mathrm{t\,yr^{-1}}$. Zehnder and North Pole B stacks ran intermittently (non-continuous) during the campaign and more frequently in February than in January (Fig. A2) due to having "limited operation" controls. ADEC (2020) provides more information on control strategies for each of the power plant facilities.

Appendix B: Evaluation of EPA-WRF model results against meteorological observations

Evaluation of the EPA-WRF simulation generally found that when surface measurements are assimilated, the errors at sites not included in the nudging also decrease. For example, root mean square error (RMSE) temperature profile errors, compared to FAI radiosondes, are as low as can be expected for a 2-month simulation with errors at or below 1 K throughout the troposphere. RMSEs of near-surface temperatures (2, 3, 6, 11, and 23 m) are 2 K or less over the full ALPACA-2022 campaign, with multiple sites having RMSEs of 1.5 K or less. Given the difficulties in simulating the winter climate of the Fairbanks area, the model performs well (Gilliam et al., 2023). Statistical evaluation of temperature profiles and SBI/EI diagnosis performed by Fochesatto et al. (2023) confirms the good model performance in terms of vertical temperature profiles. Wind speed and direction biases are larger below 150 m (up to $2.5\,\mathrm{m\,s^{-1}}$) than above the inversion layer (up to $1.5\,\mathrm{m\,s^{-1}}$). The 10 m wind speed RMSEs at the observation sites, including FAI and CTC, are closer to $1.5\,\mathrm{m\,s^{-1}}$, with direction errors around 35° (Gilliam et al., 2023). Near-surface wind errors are important considerations for this study when evaluating the transport of surface emission tracers.
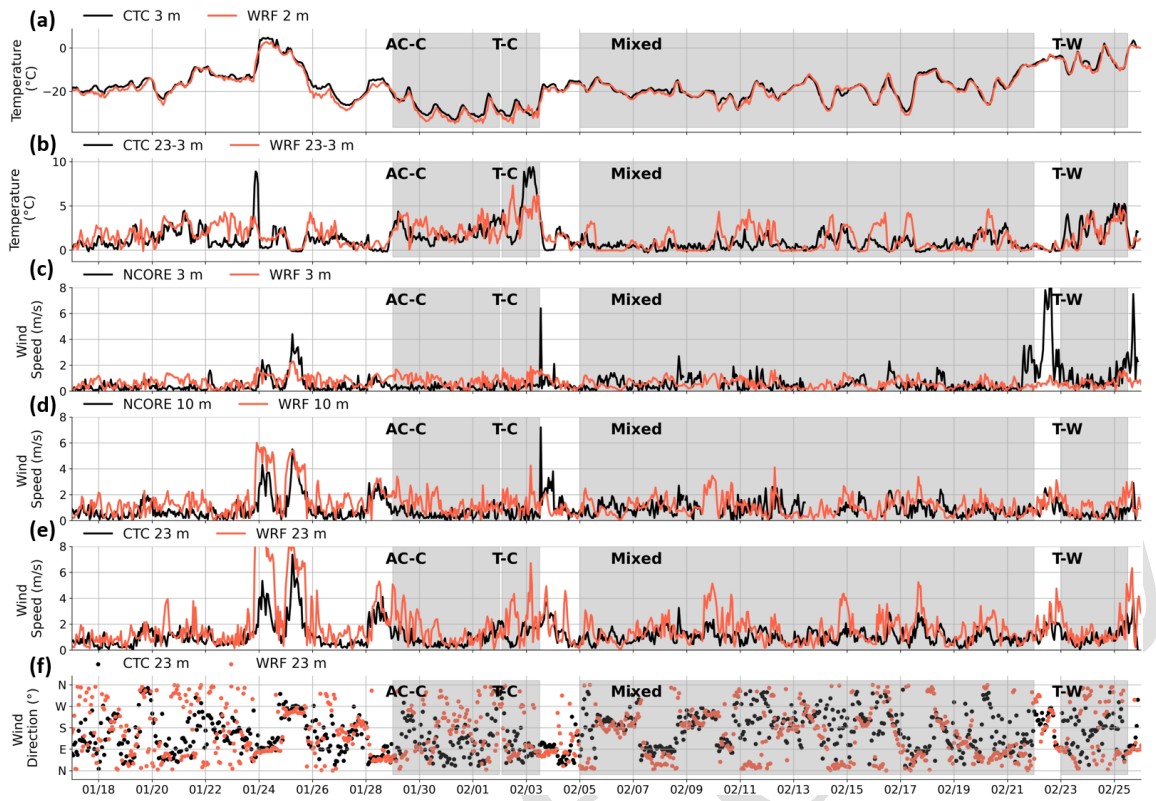
Figure B1. Time series of surface and near-surface temperatures (°C), temperature gradients (dT, °C), wind speeds (m s^{-1}), and directions (°) Downtown compared to EPA-WRF (red) for available observations (black) up to 23 m altitude during ALPACA-2022.
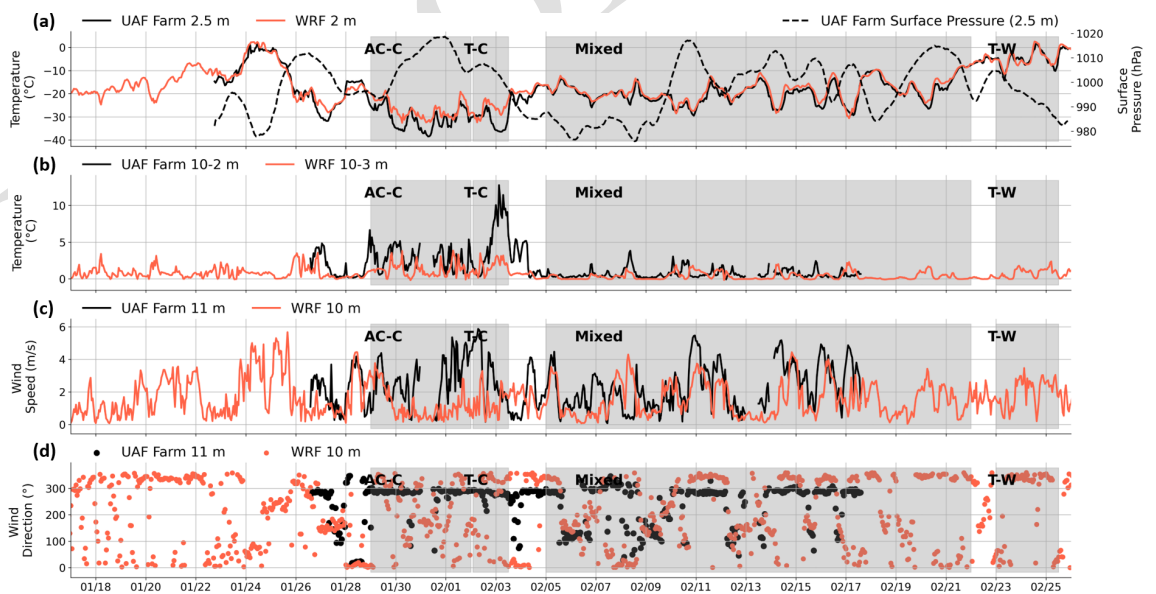
Figure B2. Time series of surface and near-surface temperatures (°C), temperature gradients (dT, °C), wind speeds (m s^{-1}), and directions (°) at the UAF Farm compared to EPA-WRF (red) for available observations (black) up to 11 m altitude during ALPACA-2022.

Figures B1 and B2 compare modelled and observed meteorology (temperatures, wind speeds, and directions) as a function of time for available altitudes up to 23 m at the Downtown and UAF Farm sites, respectively. The general variability is well captured by EPA-WRF, especially Downtown. However, for temperature gradients (23–3 m) Downtown, there are some days in which high temperature gradients are underestimated (e.g. 2 February) or overestimated (e.g. 24 January). Wind direction agreement is poor when wind speeds are very low, but this is expected owing to higher uncertainties at low wind speeds (Figs. B1f, B2d). At the UAF Farm, the very high observed temperature gradients during AC–C and T–C are underestimated by EPA-WRF. Wind speeds at the UAF Farm are in poorer agreement when temperature gradients are high, especially during AC–C and T–C. Effectively modelling local flows, as experienced at the UAF Farm, is challenging (see discussion in Sect. 6.1). Discrepancies in winds and temperatures may contribute to differences between the FLEXPART-WRF tracer concentrations and observations. This is considered in the main text.

Appendix C: Vertical and horizontal dispersion of emission tracers

Figures C1 and C2 show spatial distributions in total (surface-emitted plus power plant) tracer enhancements at various altitude levels for SO_2, CO, and NO_x. In Fig. C1, above 50 m, power plant influences are less evident for CO than for SO_2 and NO_x, with respect to the total tracer because CO emissions from power plants are smaller relative to surface-emitted tracers. For example, there is an order of magnitude difference between surface-emitted and power-plant-modelled CO tracers, which is not seen for SO_2 and NO_x (depicted in Fig. C3b; see the following). At 0–10 m, NO_x spatial variability is comparable to that of CO due to similarities in emission sources (see also Fig. A1). NO_x mixing ratios are larger from 0–100 m in SS compared to WS conditions, while above 100 m, mixing ratios are larger in WS conditions, and influences from power plants are evident (Fig. C2). The North Pole power plant stacks have larger influences on NO_x than on CO and SO_2 due to differences in fuel types. Figure C3 shows simulated power plant (i) and surface-emitted (ii) tracers as a function of altitude and time for SO_2 at Hamilton Acres and CO at the UAF Farm. Power plant contributions vary at HA and the UAF Farm, indicating influences from different power plants at each location. Vertical transport is stronger at the UAF Farm site, especially for the surface-emitted tracers (Fig. C3b).
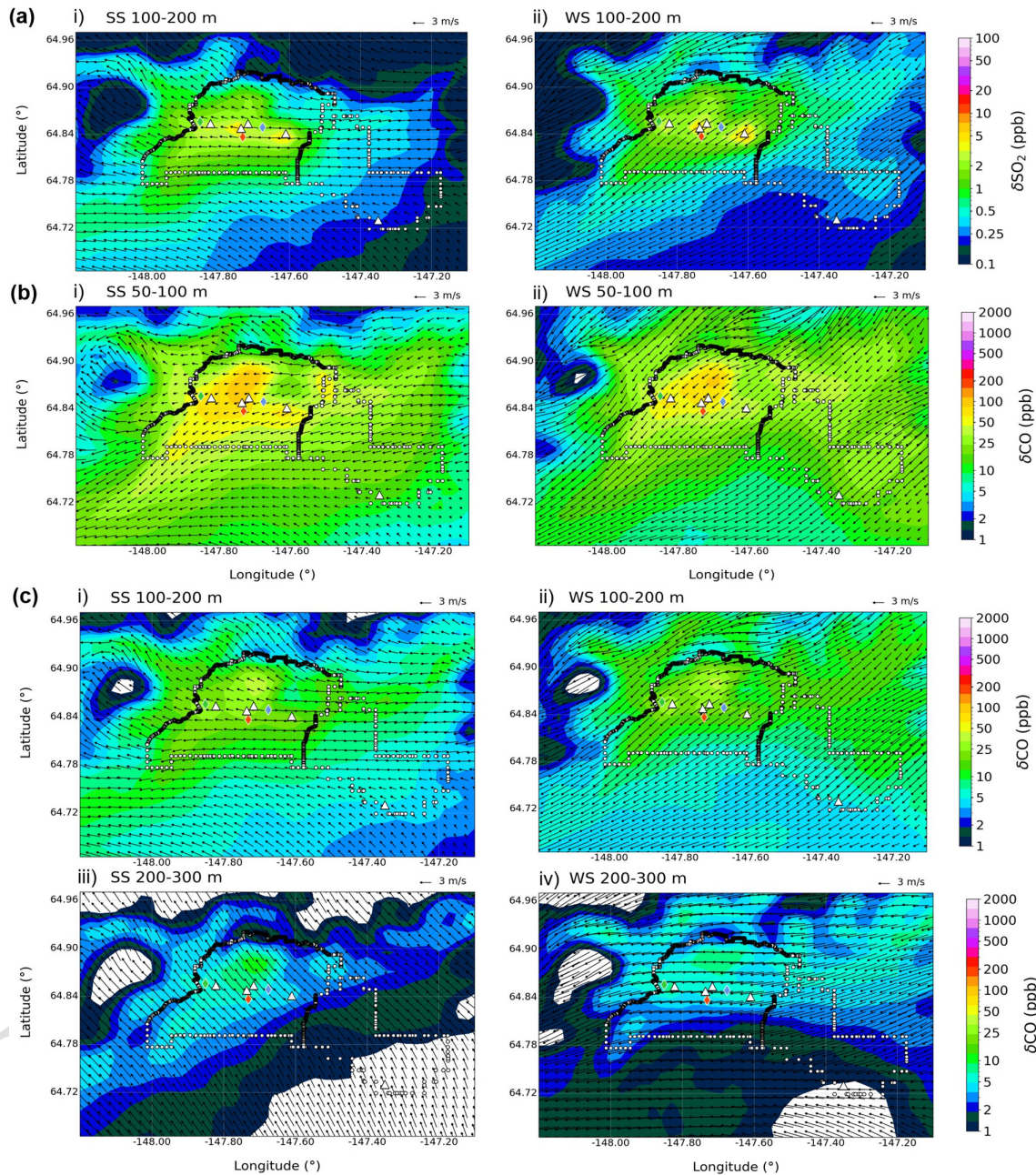
Figure C1. Spatial maps of total power plants and surface-emitted tracer enhancements (CTRL simulation) for (i) SS and (ii) WS conditions for **(a)** SO_2 (ppb) at 100–200 m, **(b)** CO at 50–100 m, and **(c)** CO at 100–200 and 200–300 m (iii, iv). Wind vectors (black arrows) indicate average wind direction (°) and wind speeds (m s^{-1}) simulated by EPA-WRF.
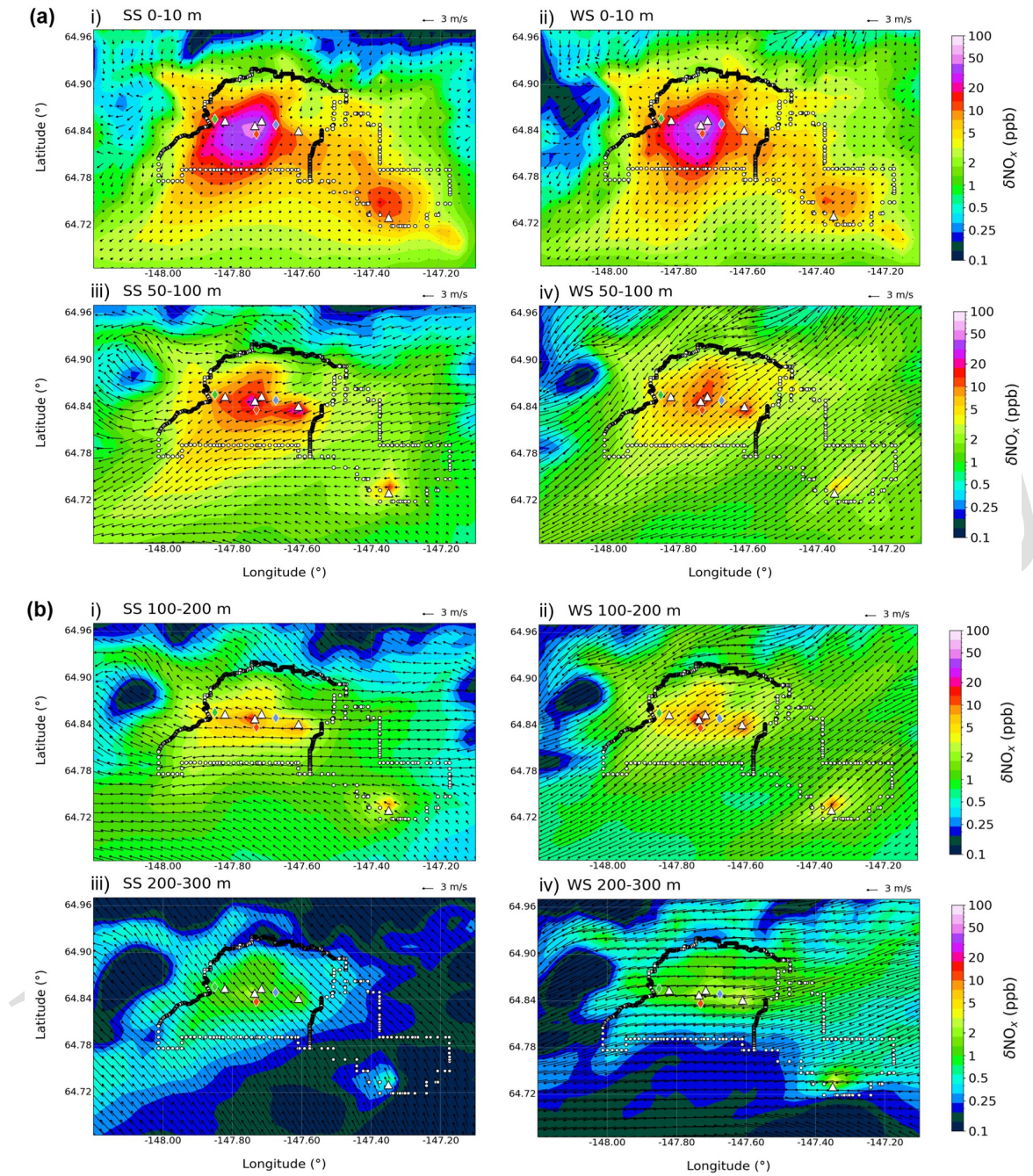
Figure C2. Spatial maps of total power plants and surface-emitted tracer enhancements (CTRL simulation) for (i) SS and (ii) WS conditions for CO (ppb) at **(a)** 0–10 m (top), 50–100 m (lower), and **(b)** 100–200 m (top) and 200–300 m (lower). Wind vectors (black arrows) indicate average wind direction (°) and wind speeds (m s^{-1}) simulated by EPA-WRF.
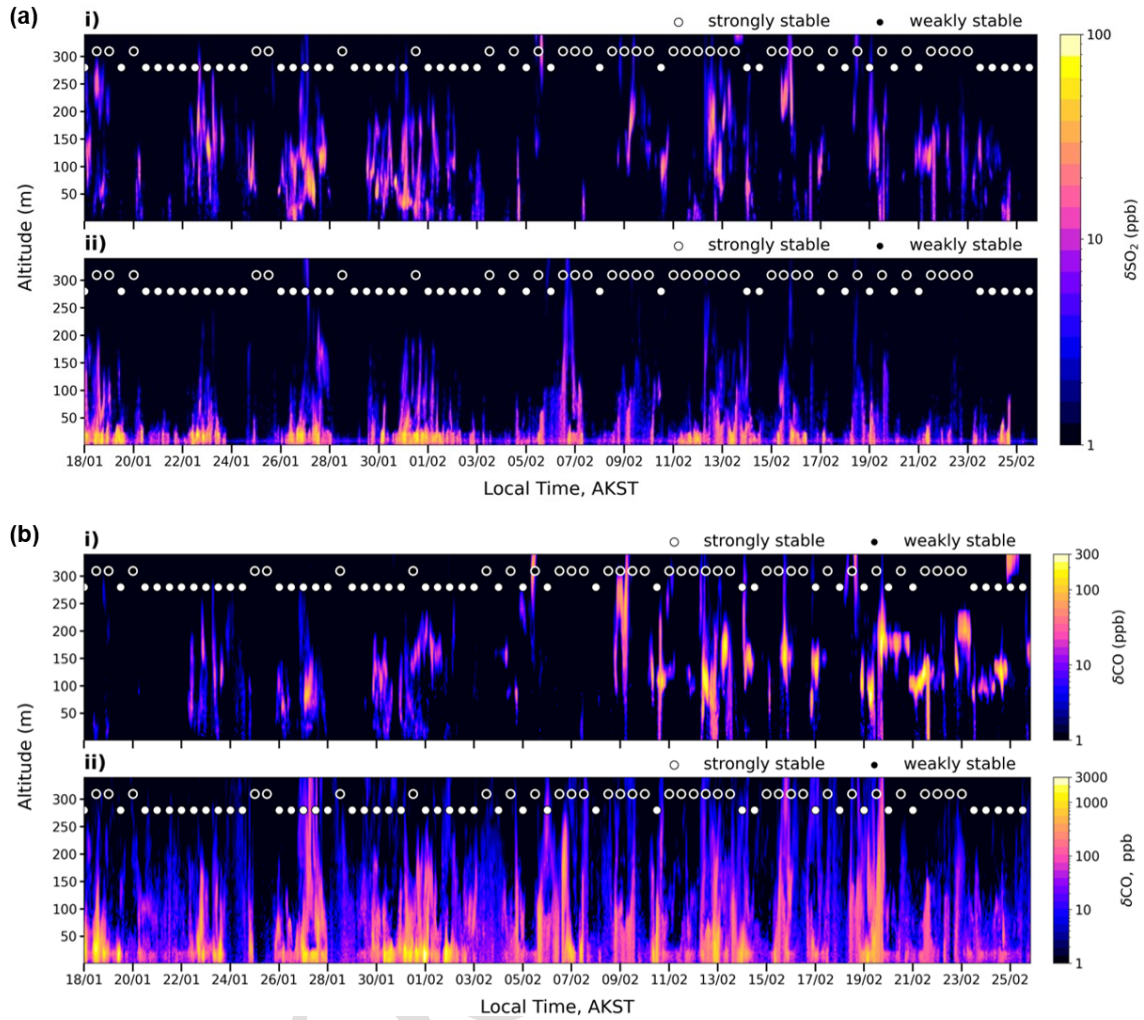
Figure C3. (a) Total power plants (i) and surface-emitted (ii) tracer enhancements (CTRL simulation) as a function of altitude and time for **(a)** SO_2 (ppb) at Hamilton Acres and **(b)** CO (ppb) at the UAF Farm. The WS and SS stability regimes are indicated every 12 h.

Appendix D: Simulated vertical distributions and power plant plumes

Vertical distributions of CO and NO_x power plant tracers as a function of time at the UAF Farm (one grid cell) of δCO and δNO_x are shown for NO-RISE and NO-CAP simulations in Fig. D1. The altitude and concentration of the model-simulated tracers compared to observed plumes are significantly improved in NO-CAP compared to NO-RISE, highlighting the importance of accounting for plume buoyancy. CTRL (Fig. 6, main text) vs. NO-CAP differences are evaluated in the main text in more detail for individual cases. In some cases (e.g. case 3, main text, and case 4, D1), the observed plume is not simulated at the grid cell closest to the UAF Farm due to displacement induced by wind direction discrepancies (see Appendix D1).

D1   Power plant plume model displacement

Figure D2a shows the spatial distribution of power plant tracers during case 3 for CO and NO_x to support the discussion in Sect. 5. Here, the larger modelled CO enhancements are supported by the influence of the UAF C stack in close proximity to the UAF Farm and a displacement of the plume from the Aurora and Zehnder stacks in the east of Fairbanks, with larger NO_x concentrations. Figure D2b shows results for an additional case study (case 4) on 3–4 February, which support the displacement of power plant tracers due to the EPA-WRF model against observation discrepancies. In Fig. D2b, there is a large underestimation of NO_x compared to observations, averaged over altitude bins. This can be explained by a discrepancy in the modelled wind direction (model: northeast, observed: east), leading to displacement of the modelled plume, as depicted in Fig. D2c. A simulated plume is transported from the Doyon stack and south of the UAF Farm site between 120–180 m at 02:00 AKST. The UAF C stack did not run during this flight (operations started from 09:00 AKST on 4 February, Sect. 2.1.1).

D2   Model evaluation against wind lidar observations

Figure D3 shows modelled power plant NO_x tracer enhancements compared to wind lidar observations measured at the CTC site (case 1 on 30 January to 1 February) and the UAF Farm (case 2 on 8 to 9 February). The wind lidar measures the three wind components using five beams (one vertical and four slanted) of infrared light to record the attenuated backscatter of particles in the air (aerosol and water droplets) between 40 and 290 m (20 m depth layers), referred to here as the range-corrected signal (RCS) (Fig. D3, panel iii) (Dieudonné et al., 2024). The quality of the signal to noise ratio depends on the presence of particles in the atmosphere; i.e. higher pollution or precipitation (snow) produces a stronger signal. A wind lidar plume mask has been developed to distinguish between water droplets and aerosols based on RCS and is used here to explore the presence of elevated plumes containing aerosols compared to the model results (Fig. D3, panel iv). This comparison is qualitative since the model simulations are enhancements in trace gas mixing ratios above background, and wind lidar RCS provides an indication of the presence of particles between 0.5–1 μm with a peak of sensitivity around 0.7–0.8 μm (Dieudonné et al., 2024), which could be either primary or secondary aerosols.
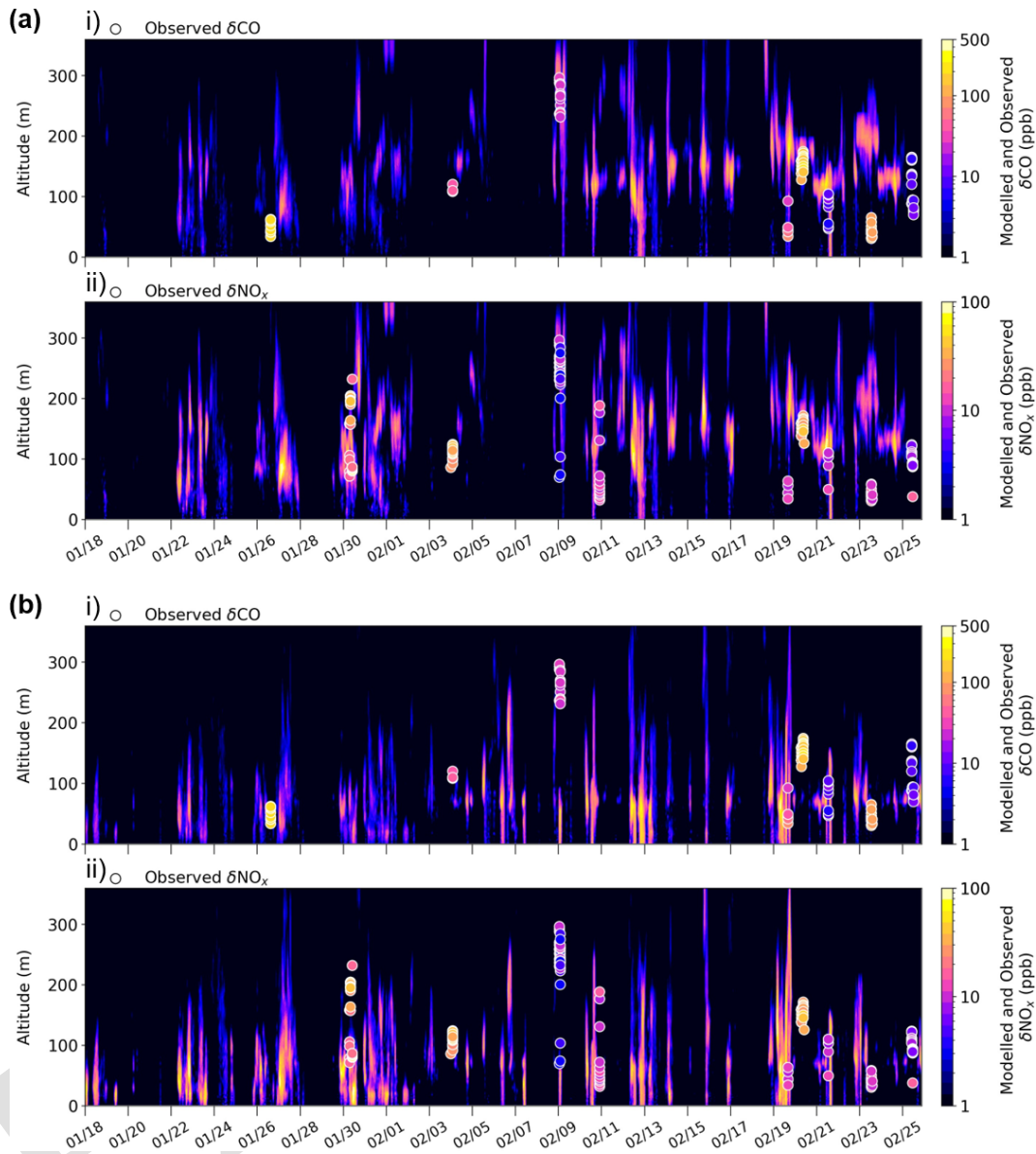
Figure D1. Comparison of modelled (CTRL) power plant and observed trace gas enhancements above background ($> 30 \, \text{m}$) for **(a)** NO-CAP and **(b)** NO-RISE and (i) δCO (ppb) and (ii) δNO_x (ppb) at the closest grid cell to the UAF Farm. Periods with available observations are shown. Observed plume enhancements are shown as circles (ppb).
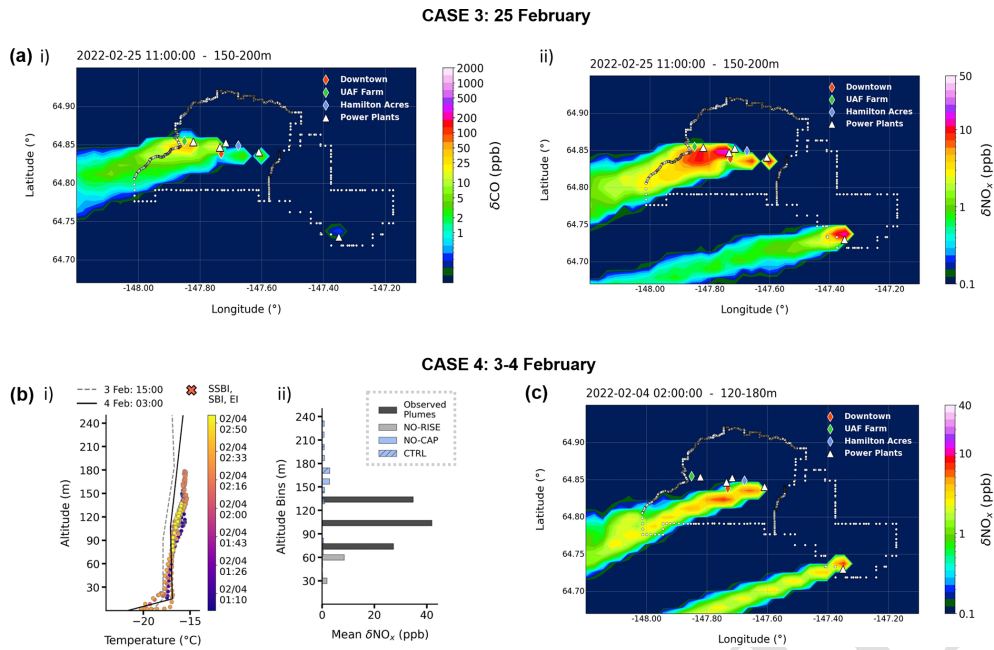
CASE 3: 25 February

CASE 4: 3-4 February

Figure D2. (a) Spatial distribution of power plant tracers for (i) CO (ppb) and (ii) NO_x (ppb) between 150–200 m at 11:00 AKST on 25 February (case 3, Sect. 5), highlighting the Aurora plume displacement to the south of the UAF Farm. **(b)** Observed temperature profiles and modelled NO_x tracer (ppb) enhancements against observations averaged over 30 m altitude bins for case 4 on 3–4 February (see Fig. 7 for details). **(c)** Spatial distribution of power plant NO_x tracer (ppb) between 120–180 m at 02:00 AKST on 4 February, highlighting the Doyon plume displacement to the south of the UAF Farm.
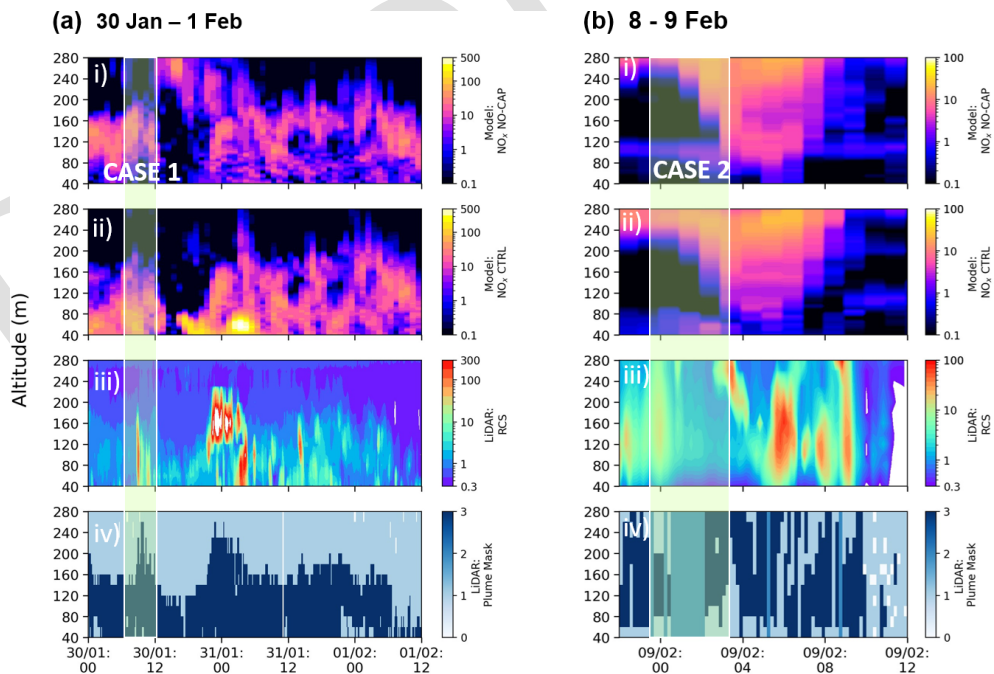
Figure D3. (i, ii) Simulated power plant NO_x tracers (ppb) as a function of altitude and time for the NO-CAP and CTRL simulations, respectively. (iii) Aerosol backscatter coefficient observed by wind lidar observations and (iv) lidar plume mask (described in Appendix D), for **(a)** 30 January to 1 February in the Downtown area (case 1, highlighted by the white box) and **(b)** 8 to 9 February at the UAF Farm (case 2, highlighted by the white box).

Appendix E: Evaluation of modelled surface tracers

E1 Statistical metrics

To evaluate model performance, normalised mean biases (NMBs) and normalised mean errors (NMEs) are calculated using the following equations, where M is the model and X is the observations:

$$\text{NMB} = \frac{\sum_{i=1}^{n}(M_i - X_i)}{\sum_{i=1}^{n} X_i}, \tag{E1}$$

$$\text{NME} = \frac{\sum_{i=1}^{n}|M_i - X_i|}{\sum_{i=1}^{n} X_i}. \tag{E2}$$

E2 UAF Farm and Hamilton Acres

NMBs and NMEs for model performance compared to surface observations are provided for the Downtown area (Table 5) and here for the HA and UAF Farm sites (Tables E1 and E2). Figures E1 and E2 show the time series and diurnal cycles for the different meteorological regimes as described in Sect. 6.1 for HA and the UAF Farm, respectively.

E3 SO$_2$ wet and dry deposition

Dry and wet deposition was explored initially and included in the CTRL simulation for SO$_2$. With regard to dry deposition of SO$_2$, fluxes are expected to be low in Arctic winter due to lower temperatures, less exposure to moist surfaces, and low levels of oxidants, as found in the Athabasca oil sands region in Canada (Hsu et al., 2016). However, Hsu et al. (2016) recorded higher deposition fluxes close to emission sources such as power plants. In this study, a dry deposition velocity of 0.1 cm s^{-1} is used, based on values recorded over snow in the wintertime Arctic, ranging from 0.06 to 0.082 cm s^{-1} (Dasch and Cadle, 1986; Valdez et al., 1987) and 0.2 cm s^{-1} in northern Canada between February and March (Barrie and Walmsley, 1978). A simplified treatment for wet deposition of SO$_2$ is also included in the CTRL run using FLEXPART-WRF. A wet deposition velocity (or scavenging coefficient) is prescribed as 1×10^{-4}, together with a Henry's law constant of 3×10^{-4}, based on values used in other studies (e.g. Valdez et al., 1987; Choi et al., 2000; Elperin et al., 2013). In general, most of the precipitation occurred during the Mixed period in February and during WS conditions. Biases were reduced when deposition was considered but had a minor effect compared to the other sensitivities in this study; hence deposition was included in the CTRL simulation.

E4 Sensitivity to vehicle NO$_x$ emissions at cold temperatures

MOVES3 (U.S. EPA, 2021) includes an incremental temperature dependence, with higher emissions at colder temperatures for petrol and diesel vehicles based on MOVES2014b (U.S. EPA, 2015). Updates in MOVES3 compared to MOVES2014b include reduced NO$_x$ emissions due to the diesel fleet turnover but not to the temperature adjustments for the trace gas species in this study. For start energy combustion emissions (from engine fuel ignition), there is a higher increment for petrol emissions at colder temperatures (up to a factor of 4.8 at $-30\,^{\circ}$C) than for diesel (up to a factor of 2.7 at $-30\,^{\circ}$C). A multiplicative adjustment using a log-linear fit based on ambient temperatures is applied to CO petrol emissions. However, for NO$_x$ petrol emissions, at $-18\,^{\circ}$C a 1.227 additive temperature adjustment is reduced to only 1.201 at $-30\,^{\circ}$C so that the adjustment does not exceed 1.2 at colder temperatures. Since NO$_x$ emissions from petrol vehicles are much lower than for CO, this results in a much higher increment for CO emissions at cold temperatures. In addition, for diesel vehicle cold starts, no statistical relationship was found for both NO$_x$ and CO, and the temperature adjustments are set to zero in MOVES3 following U.S. EPA (2015). However, data were only collected down to $+1.5\,^{\circ}$C in that study. While diesel CO emissions were not statistically significant, NO$_x$ diesel emissions were a factor of 2.6 higher at this temperature compared to a factor of 0.32 at 7 $^{\circ}$C. This, together with other studies discussed in Sect. 6.2.2, suggests that a much higher increment may be required for temperatures below 0 $^{\circ}$C. Figure E3 shows the log-linear function used to increase mobile NO$_x$ emissions based on decreases in daily average ambient temperatures.

E5 Sensitivity to photochemical lifetimes

This section investigates the influence of photochemical lifetimes on simulated tracers. The photochemical lifetime of SO$_2$ is considered, but it is estimated to be long, around 10 to 20 d, since hydroxyl radical (OH) concentrations, one of the main loss pathways for SO$_2$, are very low in Arctic winter (Yu et al., 2018; Green et al., 2019). Therefore, it is considered that transport and emissions of SO$_2$ are more important than photochemical loss during winter. The lifetime of CO is of the order of months during Arctic winter (AMAP, 2021) and is not considered further.

However, a photochemical lifetime for NO$_x$ is considered and included in the run with temperature-dependent diesel vehicle emissions (run NOx_Emissions_LT). NO is lost by reaction with O$_3$ and reformed following photolysis of NO$_2$, but in winter O$_3$ is fully or almost fully titrated since photolysis rates are very low, especially under conditions with strong surface-based temperature inversions with little vertical mixing of O$_3$ from aloft. Here, the lifetimes of NO and NO$_2$ are included and assumed to have a longer lifetime in SS compared to WS conditions. During polluted SS conditions, O$_3$ concentrations are very low or even zero at the surface, and NO$_x$ levels are high, while during WS conditions, O$_3$ is higher and mixed down from aloft, contributing to reduced NO$_x$ (Simpson et al., 2024). Kenagy et al. (2018) found that winter nighttime lifetimes were shorter (6.3 h) than those of daytime (29 h) due to the occurrence of nocturnal chemistry,

such as nitric acid and N_2O_5 production. However, if O_3 concentrations are very low, N_2O_5 formation is limited (Fibiger et al., 2018). In our study, lifetimes are assumed to be 8 and 12 h for NO and NO_2, respectively, in WS conditions and 48 h for both species in SS conditions, in line with typical winter values and increased in SS conditions to account for titrated O_3. Inclusion of NO_x lifetimes reduces the NMB and NME arising from inclusion of the temperature-dependent vehicle emissions, especially during the Mixed period (with NMB and NME reduced from 0.59 and 0.93 to -0.21 and 0.7, respectively, Table 5).

E6 Sensitivity to vertical mixing

The model is run including all previous updates (Table 4). As described earlier, h_{min}, which is used as a proxy for the height of surface stable layers in this study, is set to 20 m in CTRL. Thus, tracers that are emitted from sources at or below 20 m can be mixed up to this height if the FLEXPART-WRF ABL height is less than this, as depicted in Fig. 5. Since the structure of stable layers in the ABL is complex, sometimes with very shallow SBIs or SSBIs within SBI layers, and difficult for models to reproduce, a sensitivity run is performed with h_{min} equal to 10 m (MixH_10). However, during the Mixed period (WS conditions), the ABL is less stable with more vertical mixing. To explore this, a sensitivity with h_{min} equal to 100 m is also performed (run MixH_100). Results from MixH_100 and MixH_10 for selected periods are shown in Fig. 9, with NMBs and NMEs for all runs in Table 5.

CE14 CO and NO_x are overestimated compared to the observations during AC–C in the runs with $h_{min} = 10$ m, also seen in the diurnal comparisons, leading to poorer agreement compared to CTRL CO and NOx_Emissions_LT (Fig. 9). Results are worse for SO_2 due to excessive trapping of space heating emissions below 10 m. In contrast, on-road emissions for NO_x and CO are released only at the near surface (0–4 m). Negative biases are reduced during T–C in runs using $h_{min} = 10$ m, in particular during the daytime, and also during event T–W but only slightly, and NMBs remain high (-0.62 for MixH_10_NOx, -0.45 for MixH_10_CO, Table 4). As discussed in Sect. 4.3.2, this may be explained by meteorology. Although the surface inversion strength is reproduced quite well by EPA-WRF, simulated horizontal transport is too strong during T–W below 20 m. Runs using $h_{min} = 100$ m lead to improvements (reduced positive biases, improved NMEs) during the Mixed period for CO and NO_x due to more vertical dispersion in less stable conditions. Model biases in SO_2 are generally improved when $h_{min} = 100$ m, especially the Mixed period and in T–W. The results indicate that the modelled tracers are sensitive to the vertical distribution of emissions, such as those from space heating, and the treatment of vertical dispersion and turbulence in FLEXPART-WRF.

Table E1. Comparison of normalised mean biases (NMBs) and normalised mean errors (NMEs) of model simulations (total tracers) between 0–5 m compared to surface observations at Hamilton Acres for CO and NO_x at hourly time resolution. NMBs and NMEs are given for all data and the meteorological events AC–C, T–C, Mixed, and T–W.

Simulation name	NMB					NME				
	All data	AC–C	T–C	Mixed	T–W	All data	AC–C	T–C	Mixed	T–W
CTRL CO	-0.34	-0.27	-0.59	-0.06	-0.78	0.56	0.44	0.6	0.55	0.78
CONST CO	-0.35	-0.4	-0.64	-0.05	-0.74	0.56	0.47	0.64	0.54	0.74
MixH_100_CO	-0.44	-0.43	-0.68	-0.21	-0.78	0.57	0.49	0.68	0.49	0.78
MixH_10_CO	-0.21	-0.03	-0.42	0.06	-0.74	0.55	0.46	0.5	0.61	0.75
CTRL NOx	-0.79	-0.73	-0.88	-0.69	-0.91	0.82	0.73	0.88	0.82	0.91
NOx_Emissions	-0.58	-0.27	-0.71	-0.44	-0.89	0.72	0.51	0.72	0.77	0.89
NOx_Emissions_LT	-0.65	-0.37	-0.72	-0.6	-0.9	0.73	0.53	0.73	0.73	0.9
MixH_100_NOx	-0.66	-0.51	-0.81	-0.67	-0.91	0.73	0.59	0.81	0.75	0.91
MixH_10_NOx	-0.64	-0.13	-0.57	-0.57	-0.87	0.72	0.48	0.6	0.72	0.87

Table E2. Comparison of normalised mean biases (NMBs) and normalised mean errors (NMEs) of model simulations (total tracers) between 0–5 m compared to surface observations at the UAF Farm for CO at hourly time resolution. NMBs and NMEs are given for all data and the meteorological events AC–C, T–C, Mixed, and T–W.

Simulation name	NMB					NME				
	All data	AC–C	T–C	Mixed	T–W	All data	AC–C	T–C	Mixed	T–W
CTRL CO	0.39	0.68	−0.04	0.58	−0.06	0.56	0.82	0.33	0.64	0.18
CONST CO	0.37	0.44	−0.06	0.61	0.09	0.56	0.66	0.38	0.67	0.19
MixH_100_CO	0.07	0.08	−0.17	0.22	−0.09	0.31	0.34	0.29	0.33	0.19
MixH_10_CO	0.6	1.04	0.19	0.71	0.04	0.73	1.14	0.43	0.76	0.17
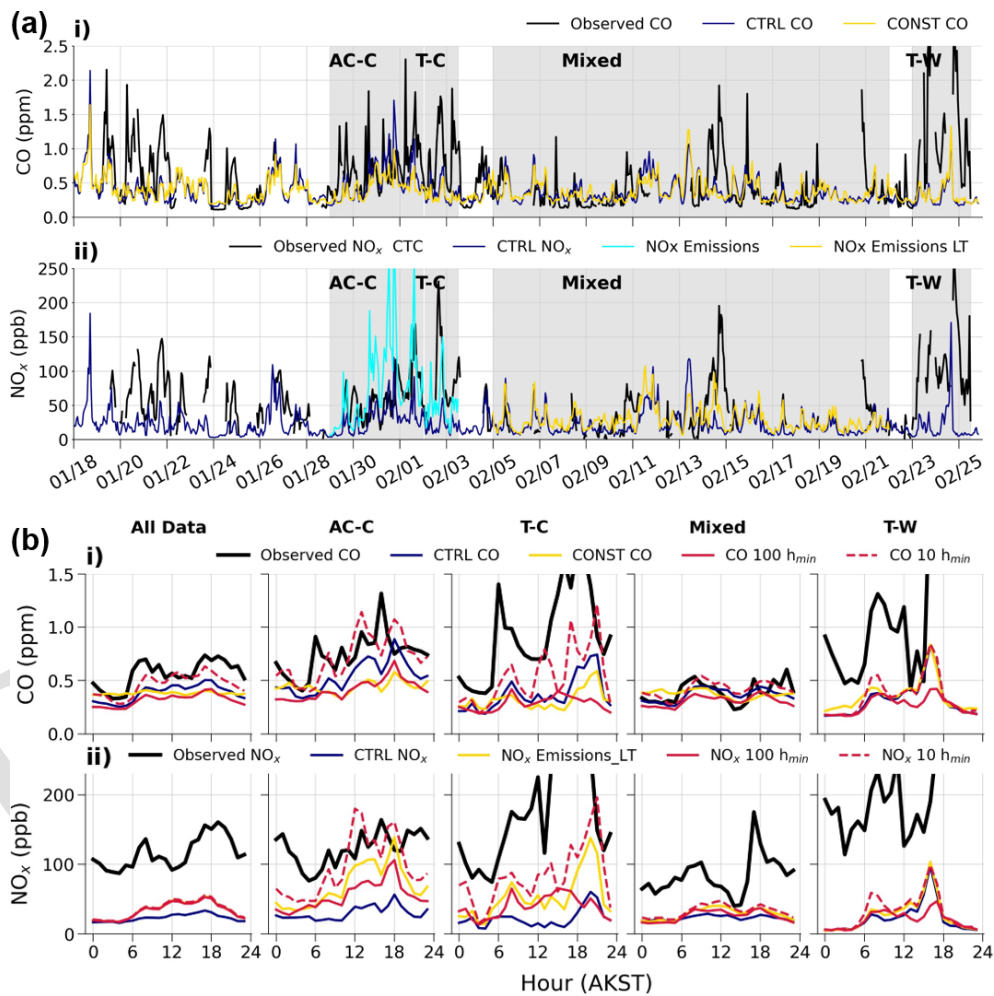
Figure E1. (a) Total modelled surface and power plant tracers as a function of time between 0–5 m for CTRL and selected sensitivity simulations described in Table 2 compared to available surface observations, at HA for (i) CO and (ii) NO_x. **(b)** Average diurnal cycles at HA for observations (black) and model simulations (colours as in **a**) for (i) CO and (ii) NO_x, averaged over all data and for events AC–C, T–C, Mixed, and T–W.
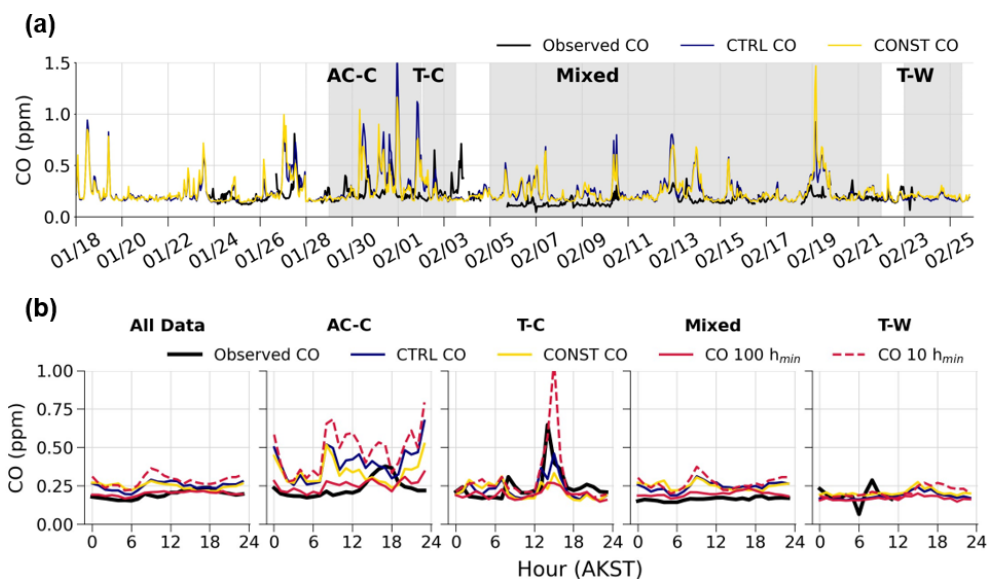
Figure E2. (a) Total modelled surface and power plant tracers as a function of time between 0–5 m for CTRL and selected sensitivity simulations described in Table 2 compared to available surface observations, at the UAF Farm for CO. **(b)** Average diurnal cycles at the UAF Farm for observations (black) and model simulations (colours as in **a**) for CO averaged over all data and for events AC–C, T–C, Mixed, and T–W.
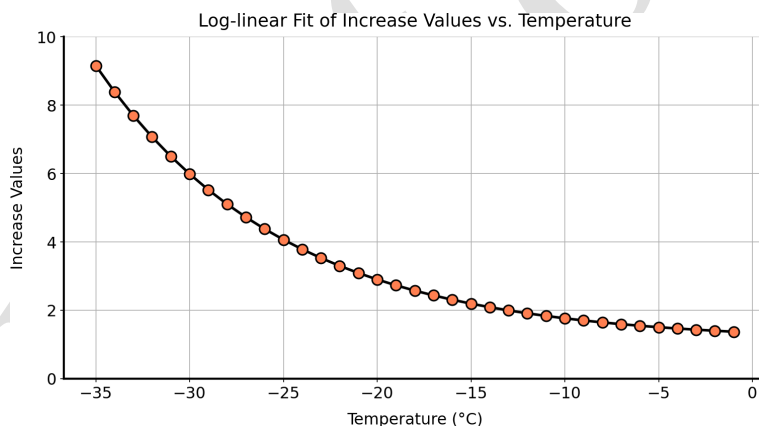
Figure E3. Increment applied to NO_x mobile (on-road and off-road) emissions as a function of daily average temperature (°C) using a log-linear function.

and simulation name lists can be requested from Robert Gilliam (gilliam.robert@epa.gov). CE15

Competing interests. The contact author has declared that none of the authors has any competing interests.

Disclaimer. The views expressed in this article are those of the authors and do not necessarily represent the views or policies of the US Environmental Protection Agency.

Publisher's note: Copernicus Publications remains neutral with regard to jurisdictional claims made in the text, published maps, institutional affiliations, or any other geographical representation in this paper. While Copernicus Publications makes every effort to include appropriate place names, the final responsibility lies with the authors.

Review statement. This paper was edited by Chris Wilson and reviewed by three anonymous referees.

References

ADEC: Amendments to: State Air Quality Control Plan, Vol. III: Appendix III.D.7.07, Alaska Department of Environmental Conservation (ADEC), 2019.

ADEC: Amendments to: State Air Quality Control Plan, Vol. II: III.D.7.07 Control Strategies, Alaska Department of Environmental Conservation (ADEC), https://dec.alaska.gov/ (last access: 3 December 2024), 2020.

ADEC: Technical Analysis Modeling Report for Phase 1, 2, and 3, Alaska Department of Environmental Conservation (ADEC) – Division of Air Quality, https://dec.alaska.gov/ (last access: 3 December 2024), 2023.

Akingunola, A., Makar, P. A., Zhang, J., Darlington, A., Li, S.-M., Gordon, M., Moran, M. D., and Zheng, Q.: A chemical transport model study of plume-rise and particle size distribution for the Athabasca oil sands, Atmos. Chem. Phys., 18, 8667–8688, https://doi.org/10.5194/acp-18-8667-2018, 2018.

Alexander, B., Allman, D., Amos, H., Fairlie, T., Dachs, J., Hegg, D. A., and Sletten, R. S.: Isotopic constraints on the formation pathways of sulfate aerosol in the marine boundary layer of the subtropical northeast Atlantic Ocean, J. Geophys. Res.-Atmos., 117, D06304, https://doi.org/10.1029/2011JD016773, 2012.

AMAP: Arctic climate change update 2021: key trends and impacts. Summary for policy-makers, Arctic monitoring and assessment programme (AMAP), p. 16, https://www.amap.no/documents/doc/arctic-climate-change-update-2021-key-trends-and-impacts.-summary-for-policy-makers/3508 (last access: 3 December 2024) 2021.

Andrew, R.: Socio-Economic Drivers of Change in the Arctic. AMAP Technical Report No. 9 (2014)., Arctic Monitoring and

Assessment Programme (AMAP), ISBN 978-82-7971-086-8, 2014.

Angevine, W. M., Baltink, H. K., and Bosveld, F. C.: Observations of the morning transition of the convective boundary layer, Bound.-Lay. Meteorol., 101, 209–227, https://doi.org/10.1023/A:1019264716195, 2001.

AQFairbanks, Program Boundaries, AQ Fairbanks, https://www.aqfairbanks.com/338/Program-Boundaries, last access: 3 December 2024.

Arctic Data Center: ALPACA Data Portal, Arctic Data Center [data set], https://arcticdata.io/catalog/portals/ALPACA/Data, last access: 3 December 2024.

Barret, B., Medina, P., Brett, N., Pohorsky, R., Law, K., Bekki, S., Fochesatto, G. J., Schmale, J., Arnold, S., Baccarini, A., Busetto, M., Cesler-Maloney, M., D'Anna, B., Decesari, S., Mao, J., Pappaccogli, G., Savarino, J., Scoto, F., and Simpson, W. R.: Vertical profiles and surface distributions of trace gases (CO, O_3, NO, NO_2) in the Arctic wintertime boundary layer using low-cost sensors during ALPACA-2022, EGUsphere [preprint], https://doi.org/10.5194/egusphere-2024-2421, 2024a.

Barret, B., Pohorsky, R., Fochesatto, J., Law, K., and Schmale, J.: Multi-platform trace gas (CO, O_3, NO, NO_2) data from the MICROMEGAS low-cost sensors instrument in Fairbanks during the Alaskan Layered Pollution and Chemical Analysis (ALPACA) field campaign in winter 2022, Arctic Data Center [data set], https://doi.org/10.18739/A2V11VN3Z, 2024b.

Barrie, L. and Walmsley, J.: A study of sulphur dioxide deposition velocities to snow in northern Canada, Atmos. Environ, 12, 2321–2332, 1978.

Benjamin, S. G., Grell, G. A., Brown, J. M., Smirnova, T. G., and Bleck, R.: Mesoscale weather prediction with the RUC hybrid isentropic–terrain-following coordinate model, Mon. Weather Rev., 132, 473–494, https://doi.org/10.1175/1520-0493(2004)132<0473:MWPWTR>2.0.CO;2, 2004.

Bieser, J., Aulinger, A., Matthias, V., Quante, M., and Van Der Gon, H. D.: Vertical emission profiles for Europe based on plume rise calculations, Environ. Pollut., 159, 2935–2946, https://doi.org/10.1016/j.envpol.2011.04.030, 2011.

Bodhaine, B. A. and Dutton, E. G.: A long-term decrease in Arctic haze at Barrow, Alaska, Geophys. Res. Lett., 20, 947–950, https://doi.org/10.1029/93GL01146, 1993.

Bourgeois, Q. and Bey, I.: Pollution transport efficiency toward the Arctic: Sensitivity to aerosol scavenging and source regions, J. Geophys. Res.-Atmos., 116, D08213, https://doi.org/10.1029/2010JD015096, 2011.

Bradley, R. S., Keimig, F. T., and Diaz, H. F.: Climatology of surface-based inversions in the North American Arctic, J. Geophys. Res.-Atmos., 97, 15699–15712, https://doi.org/10.1029/92JD01451, 1992.

Briggs, G. A.: Plume rise and buoyancy effects, Atmospheric science and power production, 327–366, https://doi.org/10.2172/6503687, 1984.

Brioude, J., Arnold, D., Stohl, A., Cassiani, M., Morton, D., Seibert, P., Angevine, W., Evan, S., Dingwell, A., Fast, J. D., Easter, R. C., Pisso, I., Burkhart, J., and Wotawa, G.: The Lagrangian particle dispersion model FLEXPART-WRF version 3.1, Geosci. Model Dev., 6, 1889–1904, https://doi.org/10.5194/gmd-6-1889-2013, 2013.

Brioude et al. TS10: FLEXPART-WRF version 3.2.2, https://www.flexpart.eu/, last access: 3 December 2024.

Cesler-Maloney, M., Simpson, W. R., Miles, T., Mao, J., Law, K. S., and Roberts, T. J.: Differences in Ozone and Particulate Matter Between Ground Level and 20 m Aloft are Frequent During Wintertime Surface-Based Temperature Inversions in Fairbanks, Alaska, J. Geophys. Res.-Atmos., 127, e2021JD036215, https://doi.org/10.1029/2021JD036215, 2022.

Choi, J., Conklin, M. H., Bales, R. C., and Sommerfeld, R. A.: Experimental investigation of SO_2 uptake in snow, Atmos. Environ., 34, 793–801, 2000.

CMAS Center: SMOKE Version 5.0 User's Manual, https://www.cmascenter.org/help/documentation.cfm?model=smoke&version=5.0 (last access: 26 March 2024), 2023.

Dasch, M. J. and Cadle, S. H.: Dry deposition to snow in an urban area, Water Air Soil Poll., 29, 297–308, 1986.

de Witt, M., Stefánsson, H., Valfells, Á., and Larsen, J. N.: Energy resources and electricity generation in Arctic areas, Renew. Energ., 169, 144–156, https://doi.org/10.1016/j.renene.2021.01.025, 2021.

Dieudonné, E., Delbarre, H., Augustin, P., Fourmentin, M., Flament, P., Deboudt, K., Halif-Ngaine, S., and Cazier, F.: 'Can commercial Doppler lidars serve air quality applications? Results from a field comparison with PM10, PM2.5, and granulometric observations in a multi-influenced harbor city', Aerosol Sci. Tech., 1–15, https://doi.org/10.1080/02786826.2024.2427868, 2024.

Donateo, A., Pappaccogli, G., Famulari, D., Mazzola, M., Scoto, F., and Decesari, S.: Characterization of size-segregated particles' turbulent flux and deposition velocity by eddy correlation method at an Arctic site, Atmos. Chem. Phys., 23, 7425–7445, https://doi.org/10.5194/acp-23-7425-2023, 2023.

Elperin, T., Fominykh, A., and Krasovitov, B.: Rain scavenging of soluble gases by non-evaporating and evaporating droplets from inhomogeneous atmosphere, Meteorol. Atmos. Phys., 122, 215–226, 2013.

Emerson, E. W., Hodshire, A. L., DeBolt, H. M., Bilsback, K. R., Pierce, J. R., McMeeking, G. R., and Farmer, D. K.: Revisiting particle dry deposition and its role in radiative effect estimates, P. Natl. Acad. Sci. USA, 117, 26076–26082, https://doi.org/10.1073/pnas.2014761117, 2020.

Fibiger, D. L., McDuffie, E. E., Dubé, W. P., Aikin, K. C., Lopez-Hilfiker, F. D., Lee, B. H., Green, J. R., Fiddler, M. N., Holloway, J. S., Ebben, C., and Sparks, T. L., Wintertime overnight NO_x removal in a southeastern United States coal-fired power plant plume: A model for understanding winter NO_x processing and its implications, J. Geophys. Res.-Atmos., 123, 1412–1425, https://doi.org/10.1002/2017JD027768, 2018.

Fochesatto, G. J.: Methodology for determining multilayered temperature inversions, Atmos. Meas. Tech., 8, 2051–2060, https://doi.org/10.5194/amt-8-2051-2015, 2015.

Fochesatto, G. J., Drobinski, P., Flamant, C., Guedalia, D., Sarrat, C., Flamant, P. H., and Pelon, J.: Evidence of dynamical coupling between the residual layer and the developing convective boundary layer, Bound.-Lay. Meteorol., 99, 451–464, https://doi.org/10.1023/A:1018935129006, 2001.

Fochesatto, G. J., Brett, N., Law, K. S., Pohorsky, R., Baccarini, A., Barret, B., Pappaccogli, G., Scoto, F., Busetto, M., Dieudonné, E., Albertin, S., Bekki, S., Maillard, J., Cesler-maloney, M.,

Raut, J.-C., Ravetta, F., Atkinson, D., Keller, D., Roberts, T. J., Schmale, J., Decesari, S., Donateo, A., Doulgeris, K., Brus, D., Arnold, S., Mao, J., and Simpson, W. R.: Overview of the ALPACA-PBL Winter Field Experiment, in: The 103rd AMS Annual Meeting, Denver, United States, January 2023, https://insu.hal.science/insu-04216320 (last access: 3 December 2024), 2023.

Fochesatto, G. J., Law, K. S., Schmale, J., Decesari, S., Simpson, W., Pohorsky, R., Barret, B., Baccarini, A., Dieudonné, E., Brett, N., Gilliam, R., Keller, D., Donateo, A., Pappaccogli, G., Scoto, F., Busetto, M., Albertin, S., Bekki, S., Ravetta, F., Raut, J.-C., Cailteau-Fischbach, C., Cesler-Maloney, M., Mao, J., Arnold, S., Temime-Roussel, B., D'Anna, B., Savarino, J., Maillard, J., Ioannidis, E., Doulgeris, K., Brus, D., Atkinson, D., Petersen, E., Iwata, H., Ueyama, M., and Harazono, Y.: Meteorological Overview of the ALPACA-2022 Field Experiment: dynamical influences on boundary-layer composition in continental Arctic wintertime, B. Am. Meteorol. Soc., submitted, 2024. TS11

Gilliam, R. C., Pouliot, G., Fahey, K., Pye, H., Briggs, N., Huff, D., and Farrell, S.: Modeling the Wintertime Meteorology for the 2022 Alaskan Layered Pollution and Chemical Analysis (AL-PACA) Campaign, in: 103rd AMS Annual Meeting, AMS, The 103rd AMS Annual Meeting, Denver, United States, 10 January 2023.

Green, J. R., Fiddler, M. N., Holloway, J. S., Fibiger, D. L., Mc-Duffie, E. E., Campuzano-Jost, P., Schroder, J. C., Jimenez, J. L., Weinheimer, A. J., Aquino, J., and Montzka, D. D.: Rates of wintertime atmospheric SO_2 oxidation based on aircraft observations during clear-sky conditions over the eastern United States, J. Geophys. Res.-Atmos., 124, 6630–6649, https://doi.org/10.1029/2018JD030086, 2019.

Guevara, M., Soret, A., Arévalo, G., Martínez, F., and Baldasano, J. M.: Implementation of plume rise and its impacts on emissions and air quality modelling, Atmos. Environ., 99, 618–629, https://doi.org/10.5194/essd-13-367-2021, 2014.

Guevara, M., Jorba, O., Tena, C., Denier van der Gon, H., Kuenen, J., Elguindi, N., Darras, S., Granier, C., and Pérez García-Pando, C.: Copernicus Atmosphere Monitoring Service TEMPOral profiles (CAMS-TEMPO): global and European emission temporal profile maps for atmospheric chemistry modelling, Earth Syst. Sci. Data, 13, 367–404, https://doi.org/10.5194/essd-13-367-2021, 2021.

Hanna, S.: Applications in air pollution modeling, in: Atmospheric Turbulence and Air Pollution Modelling: A Course held in The Hague, 21–25 September, 1981, Springer, 275–310, https://doi.org/10.1007/978-94-010-9112-1_7, 1984.

Hsu, Y.-M., Bytnerowicz, A., Fenn, M. E., and Percy, K. E.: Atmospheric dry deposition of sulfur and nitrogen in the Athabasca Oil Sands Region, Alberta, Canada, Sci. Total Environ., 568, 285–295, 2016.

Iacono, M. J., Delamere, J. S., Mlawer, E. J., Shephard, M. W., Clough, S. A., and Collins, W. D.: Radiative forcing by long-lived greenhouse gases: Calculations with the AER radiative transfer models, J. Geophys. Res.-Atmos., 113, D13103, https://doi.org/10.1029/2008JD009944, 2008.

Ioannidis, E., Law, K. S., Raut, J.-C., Marelle, L., Onishi, T., Kirpes, R. M., Upchurch, L. M., Tuch, T., Wiedensohler, A., Massling, A., Skov, H., Quinn, P. K., and Pratt, K. A.: Modelling wintertime sea-spray aerosols under Arctic haze conditions, At-mos. Chem. Phys., 23, 5641–5678, https://doi.org/10.5194/acp-23-5641-2023, 2023.

Kenagy, H. S., Sparks, T. L., Ebben, C. J., Wooldrige, P. J., Lopez-Hilfiker, F. D., Lee, B. H., Thornton, J. A., McDuffie, E. E., Fibiger, D. L., Brown, S. S., and Montzka, D. D.: NO_x lifetime and NO_y partitioning during WINTER, J. Geophys. Res.-Atmos., 123, 9813–9827, https://doi.org/10.1029/2018JD028736, 2018.

Kolker, A., Garber-Slaght, R., Anderson, B., Reber, T., Zyatitsky, K., and Pauling, H.: Geothermal Energy and Resilience in Arctic Countries, Tech. rep., National Renewable Energy Lab. (NREL), Golden, CO (United States), https://doi.org/10.2172/1862005, 2022.

Law, K. S., Stohl, A., Quinn, P. K., Brock, C. A., Burkhart, J. F., Paris, J. D., Ancellet, G., Singh, H. B., Roiger, A., Schlager, H., and Dibb, J.: Arctic air pollution: New insights from POLARCAT-IPY, B. Am. Meteorol. Soc., 95, 1873–1895, https://doi.org/10.1175/BAMS-D-13-00017.1, 2014.

Lill, E., Costa, E. J., Barry, K., Mirrielees, J. A., Mashkevich, M., Wu, J., Holen, A. L., Cesler-Maloney, M., DeMott, P. J., Perkins, R., and Hill, T.: The abundance and sources of ice nucleating particles within Alaskan ice fog, J. Geophys. Res.-Atmos., 129, e2024JD041170, https://doi.org/10.1029/2024JD041170, 2024.

Liu, S., Trainer, M., Fehsenfeld, F., Parrish, D., Williams, E., Fahey, D. W., Hübler, G., and Murphy, P. C.: Ozone production in the rural troposphere and the implications for regional and global ozone distributions, J. Geophys. Res.-Atmos., 92, 4191–4207, https://doi.org/10.1029/JD092iD04p04191, 1987.

MADIS: NCEP Meteorological Assimilation Data Ingest System (MADIS), https://madis-data.ncep.noaa.gov/index.shtml (last access: 3 December 2024), 2023.

Maillard, J., Ravetta, F., Raut, J.-C., Fochesatto, G. J., and Law, K. S.: Modulation of Boundary-Layer Stability and the Surface Energy Budget by a Local Flow in Central Alaska, Bound.-Lay. Meteorol., 185, 395–414, https://doi.org/10.1007/s10546-022-00737-2, 2022.

Mailler, S., Khvorostyanov, D., and Menut, L.: Impact of the vertical emission profiles on background gas-phase pollution simulated from the EMEP emissions over Europe, Atmos. Chem. Phys., 13, 5987–5998, https://doi.org/10.5194/acp-13-5987-2013, 2013.

Malingowski, J., Atkinson, D., Fochesatto, J., Cherry, J., and Stevens, E.: An observational study of radiation temperature inversions in Fairbanks, Alaska, Polar Sci., 8, 24–39, https://doi.org/10.1016/j.polar.2014.01.002, 2014.

Mayfield, J. A. and Fochesatto, G. J.: The layered structure of the winter atmospheric boundary layer in the interior of Alaska, J. Appl. Meteorol. Clim., 52, 953–973, https://doi.org/10.1175/JAMC-D-12-01.1, 2013.

Mölders, N., Tran, H. N., Quinn, P., Sassen, K., Shaw, G. E., and Kramm, G.: Assessment of WRF/Chem to simulate sub–Arctic boundary layer characteristics during low solar irradiation using radiosonde, SODAR, and surface data, Atmos. Pollut. Res., 2, 283–299, https://doi.org/10.5094/APR.2011.035, 2011.

Moon, A., Jongebloed, U., Dingilian, K. K., Schauer, A. J., Chan, Y. C., Cesler-Maloney, M., Simpson, W. R., Weber, R. J., Tsiang, L., Yazbeck, F., and Zhai, S.: Primary Sulfate Is the Dominant Source of Particulate Sul-

fate during Winter in Fairbanks, Alaska, ACS ES&T Air, https://doi.org/10.1021/acsestair.3c00023, 2023a.

Moon, A., Jongebloed, U., Dingilian, K., Schauer, A., Chan, Y.-C., Cesler-Maloney, M., Simpson, W., Weber, R., Tsiang, L., Yazbeck, F., Zhai, S., Wedum, A., Turner, A., Albertin, S., Bekki, S., Savarino, J., Gribanov, K., Pratt, K., Costa, E., Anastasio, C., Sunday, M., Heinlein, L., Mao, J., and Alexander, B.: Fairbanks sulfate isotope measurements during ALPACA (2022), Arctic Data Center [data set], urn:uuid:0b6901ef-310c-4a32-afdd-42e274cc095b, 2023b.

Morrison, H., Thompson, G., and Tatarskii, V.: Impact of cloud microphysics on the development of trailing stratiform precipitation in a simulated squall line: Comparison of one-and two-moment schemes, Mon. Weather Rev., 137, 991–1007, https://doi.org/10.1175/2008MWR2556.1, 2009.

Mortensen, L., Hansen, A. M., and Shestakov, A.: How three key factors are driving and challenging implementation of renewable energy systems in remote Arctic communities, Polar Geography, 40, 163–185, https://doi.org/10.1080/1088937X.2017.1329758, 2017.

Nakanishi, M. and Niino, H.: Development of an improved turbulence closure model for the atmospheric boundary layer, J. Meteorol. Soc. Jpn. Ser. II, 87, 895–912, https://doi.org/10.2151/jmsj.87.895, 2009.

NCAR: Weather Research and Forecasting Model (WRF) version 4.3, GitHub, https://github.com/wrf-model/WRF/releases, last access: 3 December 2024.

Pasquill, F. and Smith, F. B.: Atmospheric diffusion, vol. 437, E. Horwood New York, NY, USA, ISBN 0853124264978085312426904702740429780470274040085312587297808531258770-470-27404-2 TS12, 1983.

Pohorsky, R., Baccarini, A., Brett, N., Barret, B., Bekki, S., Pappaccogli, G., Dieudonné, E., Temime-Roussel, B., D'Anna, B., Cesler-Maloney, M., Donateo, A., Decesari, S., Law, K. S., Simpson, W. R., Fochesatto, J., Arnold, S. R., and Schmale, J.: In situ vertical observations of the layered structure of air pollution in a continental high latitude urban boundary layer during winter, EGUsphere [preprint], https://doi.org/10.5194/egusphere-2024-2863, 2024a.

Pohorsky, R., Baccarini, A., Tolu, J., Winkel, L. H. E., and Schmale, J.: Modular Multiplatform Compatible Air Measurement System (MoMuCAMS): a new modular platform for boundary layer aerosol and trace gas vertical measurements in extreme environments, Atmos. Meas. Tech., 17, 731–754, https://doi.org/10.5194/amt-17-731-2024, 2024b.

Robinson, E. S., Cesler-Maloney, M., Tan, X., Mao, J., Simpson, W., and DeCarlo, P. F.: Wintertime spatial patterns of particulate matter in Fairbanks, AK during ALPACA 2022, Environmental Science: Atmospheres, 3, 568–580, https://doi.org/10.1039/D2EA00140C, 2023.

Rosenthal, E. and Watson, R.: Multilateral efforts to reduce black carbon emissions: A lifeline for the warming Arctic?, Review of European Community & International Environmental Law, 20, 3–10, https://doi.org/10.1111/j.1467-9388.2011.00705.x, 2011.

Schmale, J., Arnold, S., Law, K. S., Thorp, T., Anenberg, S., Simpson, W., Mao, J., and Pratt, K.: Local Arctic air pollution: A neglected but serious problem, Earth's Future, 6, 1385–1412, https://doi.org/10.1029/2018EF000952, 2018.

Schmale, J., Sharma, S., Decesari, S., Pernov, J., Massling, A., Hansson, H.-C., von Salzen, K., Skov, H., Andrews, E., Quinn, P. K., Upchurch, L. M., Eleftheriadis, K., Traversi, R., Gilardoni, S., Mazzola, M., Laing, J., and Hopke, P.: Pan-Arctic seasonal cycles and long-term trends of aerosol properties from 10 observatories, Atmos. Chem. Phys., 22, 3067–3096, https://doi.org/10.5194/acp-22-3067-2022, 2022.

Selleri, T., Gioria, R., Melas, A. D., Giechaskiel, B., Forloni, F., Mendoza Villafuerte, P., Demuynck, J., Bosteels, D., Wilkes, T., Simons, O., and Recker, P.: Measuring Emissions from a Demonstrator Heavy-Duty Diesel Vehicle under Real-World Conditions – Moving Forward to Euro VII, Catalysts, 12, 184, https://doi.org/10.3390/catal12020184, 2022.

Seo, J., Yun, B., Kim, J., Shin, M., and Park, S.: Development of a cold-start emission model for diesel vehicles using an artificial neural network trained with real-world driving data, Sci. Total Environ., 806, 151347, https://doi.org/10.1016/j.scitotenv.2021.151347, 2022.

Sharma, S., Barrie, L. A., Magnusson, E., Brattström, G., Leaitch, W., Steffen, A., and Landsberger, S.: A factor and trends analysis of multidecadal lower tropospheric observations of Arctic aerosol composition, black carbon, ozone, and mercury at Alert, Canada, J. Geophys. Res.-Atmos., 124, 14133–14161, https://doi.org/10.1029/2019JD030844, 2019.

Shaw, G. E.: The Arctic haze phenomenon, B. Am. Meteorol. Soc., 76, 2403–2414, https://doi.org/10.1175/1520-0477(1995)076<2403:TAHP>2.0.CO;2, 1995.

Simpson, W. R., Law, K., Schmale, J., Pratt, K., Arnold, S., and Mao, J.: IGAC-ALPACA, Alaskan Layered Pollution And Chemical Analysis (ALPACA) White Paper, https://igacproject.org/publication/other-publications/alaskan-layered-pollution-and-chemical-analysis-alpaca-white-paper (last access: 3 December 2024), 2018.

Simpson, W., Cesler-Maloney, M., and Hoskins-Chaddon, R.: Gas and meteorological measurements at the CTC site and Birch Hill in Fairbanks, Alaska, during the ALPACA-2022 field study, Arctic Data Center [data set], https://doi.org/10.18739/A27D2Q87W, 2023.

Simpson, W. R., Mao, J., Fochesatto, G. J., Law, K. S., DeCarlo, P. F., Schmale, J., Pratt, K. A., Arnold, S. R., Stutz, J., Dibb, J. E., Creamean, J. M., Weber, R. J., Williams, B. J., Alexander, B., Hu, L., Yokelson, R. J., Shiraiwa, M., Decesari, S., Anastasio, C., D'Anna, B., Gilliam, R. C., Nenes, A., St. Clair, J. M., Trost, B., Flynn, J. H., Savarino, J., Conner, L. D., Kettle, N., Heeringa, K. M., Albertin, S., Baccarini, A., Barret, B., Battaglia, M. A., Bekki, S., Brado, T. J., Brett, N., Brus, D., Campbell, J. R., Cesler-Maloney, M., Cooperdock, S., Cysneiros de Carvalho, K., Delbarre, H., DeMott, P. J., Dennehy, C. J. S., Dieudonné, E., Dingilian, K. K., Donateo, A., Doulgeris, K. M., Edwards, K. C., Fahey, K., Fang, T., Guo, F., Heinlein, L. M. D., Holen, A. L., Huff, D., Ijaz, A., Johnson, S., Kapur, S., Ketcherside, D. T., Levin, E., Lill, E., Moon, A. R., Onishi, T., Pappaccogli, G., Perkins, R., Pohorsky, R., Raut, J.-C., Ravetta, F., Roberts, T., Robinson, E. S., Scoto, F., Selimovic, V., Sunday, M. O., Temime-Roussel, B., Tian, X., Wu, J., and Yang, Y.: Overview of the Alaskan Layered Pollution and Chemical Analysis (ALPACA) Field Experiment, ACS EST Air, 1, 200–222, https://doi.org/10.1021/acsestair.3c00076, 2024.

Skov, H., Massling, A., Nordstrøm, C., Bossi, R., Vorkamp, K., Christensen, J. H., Hansen, K. M., Poulsen, M. B., Pernov, J. B., Thomas, D. C., and Hjorth, J. L.: AMAP CORE-ATMOSPHERE, and no. TS13 : Scientific Report from DCE–Danish Centre for Environment and Energy, ISBN: 978-87-7156-797-7, 2023.

Stohl, A.: Characteristics of atmospheric transport into the Arctic troposphere, J. Geophys. Res.-Atmos., 111, D11306, https://doi.org/10.1029/2005JD006888, 2006.

Stohl, A., Klimont, Z., Eckhardt, S., Kupiainen, K., Shevchenko, V. P., Kopeikin, V. M., and Novigatsky, A. N.: Black carbon in the Arctic: the underestimated role of gas flaring and residential combustion emissions, Atmos. Chem. Phys., 13, 8833–8855, https://doi.org/10.5194/acp-13-8833-2013, 2013.

Tran, H. N. and Mölders, N.: Investigations on meteorological conditions for elevated $PM_{2.5}$ in Fairbanks, Alaska, Atmos. Res., 99, 39–49, https://doi.org/10.1016/j.atmosres.2010.08.028, 2011.

U.S. EPA: Emission Adjustments for Temperature, Humidity, Air Conditioning, and Inspection and Maintenance for On-road Vehicles in MOVES2014, Environmental Protection Agency – Assessment and Standards Division, Office of Transportation and Air Quality, https://www.epa.gov/moves/moves-onroad-technical-reports (last access: 4 December 2024), 2015.

U.S. EPA: Overview of EPA's Motor Vehicle Emission Simulator (MOVES3), Environmental Protection Agency – Assessment and Standards Division, Office of Transportation and Air Quality, https://www.epa.gov/moves/moves-onroad-technical-reports (last access: 4 December 2024), 2021.

Valdez, M. P., Bales, R. C., Stanley, D. A., and Dawson, G. A.: Gaseous deposition to snow: 1. Experimental study of SO_2 and NO_2 deposition, J. Geophys. Res.-Atmos., 92, 9779–9787, 1987.

Wærsted, E. G., Sundvor, I., Denby, B. R., and Mu, Q.: Quantification of temperature dependence of NO_x emissions from road traffic in Norway using air quality modelling and monitoring data, Atmos. Environ. X, 13, 100160, https://doi.org/10.1016/j.aeaoa.2022.100160, 2022.

Wang, Y., Zhang, Q., Jiang, J., Zhou, W., Wang, B., He, K., Duan, F., Zhang, Q., Philip, S., and Xie, Y.: Enhanced sulfate formation during China's severe winter haze episode in January 2013 missing from current models, J. Geophys. Res.-Atmos., 119, 10–425, https://doi.org/10.1002/2013JD021426, 2014.

Weber, C., Sundvor, I., and Figenbaum, E.: Comparison of regulated emission factors of Euro 6 LDV in Nordic temperatures and cold start conditions: Diesel-and gasoline direct-injection, Atmos. Environ., 206, 208–217, https://doi.org/10.1016/j.atmosenv.2019.02.031, 2019.

Ye, L. and Wang, Y.: Long-term air quality study in Fairbanks, Alaska: Air pollutant temporal variations, correlations, and $PM_{2.5}$ source apportionment, Atmosphere, 11, 1203, https://doi.org/10.3390/atmos11111203, 2020.

Yu, T., Zhao, D., Song, X., and Zhu, T.: NO_2-initiated multiphase oxidation of SO_2 by O_2 on $CaCO_3$ particles, Atmos. Chem. Phys., 18, 6679–6689, https://doi.org/10.5194/acp-18-6679-2018, 2018.

Remarks from the language copy-editor

CE1   Due to the large number of changes requested, please carefully check that everything was modified correctly.

CE2   Please verify the slight changes made.

CE3   Because there is internal punctuation within the list (i.e. commas in "ADEC sites including NCORE (NC), A Street, and Hurst Rd"), the semi-colons are correct.

CE4   While the meaning is plural, the form is singular. "Deposition" would have to be pluralised or doubled (i.e. dry deposition and wet deposition) here and below. Please advise.

CE5   This comma was added to close the comma introducing the dependent clause starting with "measured using the...". Either this comma remains or both should be deleted. Please advise.

CE6   Please verify the caption.

CE7   A comma here would not be correct as it would separate the subject from the verb.

CE8   Please verify. I joined the sentences to make them complete.

CE9   I believe the "the" is correct here as "North Pole A" is acting as a modifier to "stack".

CE10   A–C changed to AC–C throughout. Please verify.

CE11   Please verify.

CE12   "The" was added to avoid beginning the sentence with a number. Please verify.

CE13   Please verify.

CE14   Sorry, could you please more clearly state what should be changed in these two sentences?

CE15   Please verify the section.

CE16   The period here ends the sentence.

CE17   Please verify this section noting that words of thanks like "acknowledge" are not permitted in this section.

Remarks from the typesetter

TS1   Please also carefully check the corrections in the caption of this figure as they might not show in the track changes file for technical reasons.

TS2   In line with our house standards, we do not use superscripts for th.

TS3   Due to the requested change, we would have to forward your request to the handling editor for approval. To explain the corrections needed to the editor, please send me an explanation why this correction is necessary. Many thanks.

TS4   Is it correct that there is no SRA (Steve R. Arnold) in this section and SA stands for Sarah Albertin in each case?

TS5   In line with our house standards, author names are not abbreviated in the financial support section. I changed the initials to the written-out versions of the names. Please check JS and GP in this section and let me know which author it stands for as in both cases there are two possibilities. Many thanks.

TS6   Please check.

TS7   Please check.

TS8   Please check.

TS9   Check.

TS10   Please add all authors.

TS11   It does not have to be deleted. Please let me know if you prefer it to be removed though.

TS12   Please check. Shouldn't this be 10 or 13 digits long?

TS13   Can "and no." be removed?